NATIONAL TECHNICAL UNIVERSITY OF ATHENS

DIPLOMA THESIS

Controlling Bifurcations of Fixed Point and Limit Cycle Equilibria in High-Speed Rotors Utilizing Active Gas Foil Bearings

---

Author:
Anastasios Papadopoulos

Supervisor:
Athanasios Chasalevris

A thesis submitted in fulfillment of the requirements for the degree of Diploma in Mechanical Engineering

October 19, 2022

NATIONAL TECHNICAL UNIVERSITY OF ATHENS

Abstract

Faculty Name
School of Mechanical Engineering

Diploma in Mechanical Engineering

Controlling Bifurcations of Fixed Point and Limit Cycle Equilibria in High-Speed Rotors Utilizing Active Gas Foil Bearings

by Anastasios Papadopoulos

High speed rotors on gas foil bearings (>200kRPM) are applications of increasing interest due to their potential to increase the power to weight ratio in machines and also establish oil-free design solutions. The gas lubrication principles render lower – compared to oil – power losses and increase the threshold speed of instability in rotating systems. However, self-excited oscillations may still occur at DN (Diameter [mm] X Rotating Speed [RPM]) values much lower than the speed of sound [DN<6.5e6], these being usually triggered through Hopf bifurcation of a fixed point equilibrium (fully balanced rotor) or secondary Hopf (Neimark-Sacker) bifurcation of periodic limit cycles (unbalanced rotor). Bifurcation-free operation is a target in the dynamic design of high-speed machines like automotive turbosystems, turbopumps for rocket propulsion, small jet engines for drones or UAVs, and others; this is not always achievable with conventional rotor-bearing design. In this work, an active gas foil bearing is presented as a novel configuration including a number of piezoelectric actuators which shape the foil component through linear feedback control. At first, an enhanced finite element model for the thin foil mounted in a number of PZTs, is developed in order to avoid shear lock effect. Second, the gas-structure interaction (FSI) is modeled through Reynolds equation for compressible flow. A simple rotor model consisting of a rigid rotor and 2 gas foil bearings is then defined, and the dynamic system is composed with its unique source of nonlinearity to be the nonlinear impedance forces from the gas to the rotor and to the foil. The third milestone includes a linear feedback control scheme to stabilize (pole placement) the dynamic system, linearized around a speed depended equilibrium (balanced rotor). Linear control is found to be insufficient to stabilize the system when certain perturbations apply. Further to that, unbalanced rotor systems (most common case) follow trajectories which extend far from fixed point equilibria, emerging strong nonlinear impedance forces from the bearings. Linear feedback control is applied in the dynamic system utilizing polynomial feedback functions in order to overcome the problem of instability. Case studies include a small (30mm) and a large (100mm) bearing, both at operating range with upper bound of speed at DN = 6.5e6; different foil thickness is also included in the case study.

ΕΘΝΙΚΟ ΜΕΤΣΟΒΙΟ ΠΟΛΥΤΕΧΝΕΙΟ

Περίληψη

Σχολή Μηχανολόγων Μηχανικών

Διπλωματική Εργασία

Έλεγχος διακλαδώσεων σημείων ισορροπίας και οριακών κύκλων σε περιστρεφόμενους άξονες υψηλών ταχυτήτων με χρήση ενεργών αεροεδράνων

του Αναστάσιου Παπαδόπουλου

Οι περιστρεφόμενοι άξονες υψηλών ταχυτήτων (>200kRPM) στηριζόμενοι σε αεροέδρανα αποτελούν εφαρμογές με αυξανόμενο ενδιαφέρον λόγω της δυνατότητάς τους να αυξήσουν τον λόγο απόδοσης-βάρους των μηχανών και επίσης να εγκαθιδρύσουν καθεστώς λίπανσης άνευ ελαίου (oil-free lubrication). Το φυσικό αξίωμα της αεροδυναμικής λίπανσης επιτρέπει χαμηλότερες απώλειες ισχύος σε σχέση με την υδρολίπανση και αυξάνει την ταχύτητα περιστροφής στην οποία επέρχεται αστάθεια στα περιστρεφόμενα συστήματα. Ωστόσο, αυτοδιεγειρόμενες ταλαντώσεις δύνανται να συμβούν σε τιμές DN (Διάμετρος άξονα [mm] X Ταχύτητα περιστροφής [RPM]) αρκετά χαμηλότερες από αυτή που αντιστοιχεί στην ταχύτητα του ήχου (DN<6.5e6), και αυτές συνήθως προέρχονται έπειτα από διακλάδωση Hopf σε σημείο ισορροπίας (fixed point) όταν ο άξονας είναι τέλεια ζυγοσταθμισμένος, ή Secondary Hopf (Neimark-Sacker) σε περιοδικές ή σχεδόν περιοδικές τροχιές (limit cycles) όταν ο άξονας είναι ατελώς ζυγοσταθμισμένος. Η λειτουργεία του περιστρεφόμενου συστήματος χωρίς την εμφάνιση κάποιου τύπου διακλάδωσης είναι στόχος του δυναμικού σχεδιασμού υψηλόστροφων συστημάτων όπως οι υπερτροφοδότες (turbochargers), οι στροβιλοαντλίες (turbopumps) για πυραυλική πρόωση, οι μικροί κινητήρες jet για drones ή μη επανδρωμένα αεροχήματα, και άλλα. Αυτό δεν είναι πάντα εφικτό με συμβατικά αεροέδρανα.

Σε αυτή την εργασία, ένα ενεργό αεροέδρανο (Active Gas Foil Bearing - AGFB) παρουσιάζεται ως μία καινοτόμα διαμόρφωση περιλαμβάνοντας πιεζοηλεκτρικούς διεγέρτες οι οποίοι μορφοποιούν το κέλυφος του αεροεδράνου μέσω γραμμικού ελέγχου ανάδρασης. Αρχικά παρουσιάζεται μία βελτιωμένη προσομοίωση της δυναμικής συμπεριφοράς του κελύφους χρησιμοποιώντας Πεπερασμένα Στοιχεία, καθώς αυτό στηρίζεται στους πιεζοηλεκτρικούς επενεργητές, αποφεύγοντας το φαινόμενο του shear lock. Έπειτα, η αλληλεπίδραση της ροής αερίου και της δομής του κελύφους (FSI) προσομοιώνεται μέσω της εξίσωσης Reynolds για συμπιεστό ρευστό και μαζί με τις εξισώσεις κίνησης του άξονα αποτελούν ένα ισχυρά μη-γραμμικό και αριθμητικά στιβαρό (numerically stiff) πρόβλημα. Ο περιστρεφόμενος άξονας προσομοιώνεται με ένα απλό συμμετρικό μοντέλο άκαμπτου στέρεου (rigid rotor) και στηρίζεται σε 2 πανομοιότυπα ενεργά αεροέδρανα (AGFBs) και το δυναμικό σύστημα ορίζεται με την μοναδική πηγή μη-γραμμικότητας να είναι η μη-γραμμική συνισταμένη δύναμη από το αέριο προς τον άξονα και προς το κέλυφος.

Το τρίτο μέρος της εργασίας περιλαμβάνει τον σχήμα γραμμικού ελέγχου ανάδρασης για να σταθεροποιήσει (τοποθέτηση πόλων) το δυναμικό σύστημα, το οποίο είναι γραμμικοποιημένο γύρω από μία θέση ισορροπίας (τέλεια ζυγοσταθμισμένος άξονας) εξαρτημένη από την ταχύτητα περιστροφής.

Ο γραμμικός έλεγχος ανάδρασης αποδεικνύεται ανεπαρκής για την ευστάθεια του συστήματος όταν εφαρμόζονται συγκεκριμένες διαταραχές στο σύστημα. Επιπλέον, οι αζυγοστάθμητοι άξονες (η πιο συνηθισμένη περίπτωση) εξελίσσουν τροχιές οι οποίες εκτείνονται μακριά από το σημείο ισορροπίας (fixed point) και προκαλούν έντονα μη-γραμμικές δυνάμεις εδράνων. Ο γραμμικός έλεγχος ανάδρασης εφαρμόζεται στο δυναμικό σύστημα με πολυωνυμικές συναρτήσεις ανάδρασης για να ξεπεραστεί το πρόβλημα της αστάθειας. Η μελέτη των περιπτώσεων περιλαμβάνει ένα μικρότερο (D30) και ένα μεγαλύτερο (D100) έδρανο, και τα δύο με άνω όριο ταχύτητας περιστροφής το αντίστοιχο σε DN = 6.5e6. Το διαφορετικό πάχος κελύφους συγκαταλέγεται επίσης στην μελέτη των περιπτώσεων.

Acknowledgements

This thesis is a result of 7 months of work (March 2022 - September 2022) in the Rotordynamics Group at the NTUA School of Mechanical Engineering. During its preparation, I interacted with people with a passion for the topic of Dynamics, with disciplines and with high-level knowledge that influenced me and thanks to whom I gained a more concrete and thorough view of the profession of a mechanical engineer.

First of all, I would like to thank Prof. Athanasios Chasalevris for his valuable contribution to the preparation and the implementation of this work. His constant guidance and availability as well as his willingness to pass on his knowledge were invaluable and without him the completion of this thesis would have been impossible.

Furthermore, I want to express my gratitude to PhD candidate Ioannis Gavalas for the endless hours he dedicated to supporting this thesis. Together we spent a great amount of time in the laboratory of the school in order to complete the work. Moreover, I would like to thank the MSc student Emmanuel Dimou for his decisive and vital contribution to the design of the control systems and the excellent ideas he had on the topic. I am more than happy that I was given the chance to meet people with common interests.

Finally, I would like to thank my parents and my sister for their unlimited support during these seven months, especially at times when I seemed stressed and frustrated. They were a decisive factor for the completion of both this work and my studies generally.

Dedicated to my sister…

Contents

List of Figures

List of Tables

List of Abbreviations

AGFB	**A**ctive **G**as **F**oil **B**earing
AMB	**A**ctive **M**agnetic **B**earing
DOF	**D**egree **O**f **F**reedom
FEM	**F**inite **E**lement **M**ethod
FSI	**F**luid **S**tructure **I**nteraction
GFB	**G**as **F**oil **B**earing
MBC	**M**agnetic **B**earing **C**ontroller
MZC	**M**elosh **Z**ienkiewicz **C**heung
PZT	**P**ie**z**oelec**t**ric Actuators

Nomenclature

Hellenic Letters

$\Delta\chi$	Finite differences interval length in the χ direction
Ω_{th}	Rotational speed where the Hopf bif. occurs
η	dimensionless coordinate in the y-direction
η_f	Rayleigh damping factor
λ	Eigenvalue
μ	Lubricant dynamic viscosity
ω	Natural frequency
Ω	Rotating speed
ω_d	Damped natural frequency
Ω_r	Maximum operating speed
ϕ_r	Angle of eccentricity forces
ρ	Density of the material of the foil
ρ_{air}	Density of the air
θ	Bearing angle coordinate
θ_{x_i}	rotation of the node i around the x-axis
θ_{y_i}	rotation of the node i around the y-axis
ξ	dimensionless coordinate in the x-direction

Latin Letters

δL	Enlargement of the actuator
Δz	Finite differences interval length in the z direction
$\tilde{\mathbf{x}}$	Error of the state variables
$\mathbf{B_s}$	Strain matrix
$\mathbf{B}$	Part. der. of the vector field wrt the displ. of the act.
$\mathbf{C_r}$	Reduced global damping matrix of the foil
$\mathbf{C}$	Global damping matrix of the foil
$\mathbf{D}$	Material matrix

$\mathbf{F_e}$ Force vector of the finite element

$\mathbf{f_f}$ Vector field of the foil state equations

$\mathbf{f_p}$ Vector field of the pressure state equations

$\mathbf{F_r}$ Reduced gas forces vector acting on the foil

$\mathbf{f_R}$ Vector field of the rotor state equations

$\mathbf{F_{act}}$ Forces on the foil due to displacement of the actuators

$\mathbf{F_{tot}}$ Total forces on the foil

$\mathbf{F}$ Gas forces vector acting on the foil

$\mathbf{f}$ Vector field of the full nonlinear system equations

$\mathbf{J}, \mathbf{A}$ Jacobian matrix

$\mathbf{K_e}$ Stiffness matrix of the finite element

$\mathbf{K_g}$ Gain matrix

$\mathbf{K_r}$ Reduced global stiffness matrix of the foil

$\mathbf{K}$ Global stiffness matrix of the foil

$\mathbf{L}$ Observer matrix

$\mathbf{M_e}$ Mass matrix of the finite element

$\mathbf{M_r}$ Reduced global mass matrix of the foil

$\mathbf{M}$ Global mass matrix of the foil

$\mathbf{N_i}$ Shape functions of the node i

$\mathbf{q_a}$ Vector of displacements of the actuators

$\mathbf{w_e}$ Vector of degrees of freedom of the finite element

$\mathbf{x}$ State variables of the full nonlinear system

a Half-length of the finite element in the x-direction

b Half-length of the finite element in the y-direction

c_r Bearing radial clearance

D_f, R_f Diameter and radius of the foil

d_{33} Deformation coefficient of the piezoelectric actuator

E Young's modulus of elasticity

e_u Unbalance eccentricity

F_{B_x}, F_{B_y} Gas forces on the rotor

F_{U_x}, F_{U_y} Unbalance forces

G	Shear modulus
h	Lubrication film thickness
k_i	Gain i of the polynomial feedback law
L_f	Length of the foil
m_d	Mass of the disc
n	Number of layers of the piezoelectric actuator
p	Pressure
q_i	Vertical displacement of the node i of the finite element mesh
R	Radius of the rotor
t	Time
V	Voltage
v	Poisson's ratio
w	Vertical displacement in the interior of a finite element
x_j, y_j	Displacements of the center of the disc
z	Axial coordinate of the bearing

Chapter 1

Introduction

1.1 Conventional Gas Foil Bearings

Gas foil bearings are self-acting machine elements designed to support high-speed rotating machines [1]. They utilize an oil-free technology by creating a thin load-carrying gas film, without the need for external pressurization. Furthermore, because of the absence of contact between the rotor and the internal shell of the bearing there has been found that low power loss can be achieved, as described by H. Heshmat [2].

Over the past few decades, there has been a rapid development of GFBs and their applications, especially in turbofan engines of commercial aircraft [3]. Moreover, there is an ever-increasing interest in the application of GFBs in turbocharging systems [4].

The resemblance between foil bearings and oil-lubricated bearings is great in terms of their size, shape and utilization of the hydrodynamic effect to develop the fluid film pressure. However, the working mean of GFBs is the air and their inner shell is deformable, in comparison with oil bearings, where their inner surface is rigid [5]. This inner shell of foil bearings, also named top foil, is a thin shell supported by a pack of spring-like layers, called bump foil. As a result, the bearing is adjustable to potential shaft misalignment and thermal deformation and the user is given the option to preload the bearing in such a way, in order to achieve the desired film pressure and, as a result, the desired load capacity [6]. The schematic representation of oil bearings and gas foil bearings is shown in Fig 1.1.

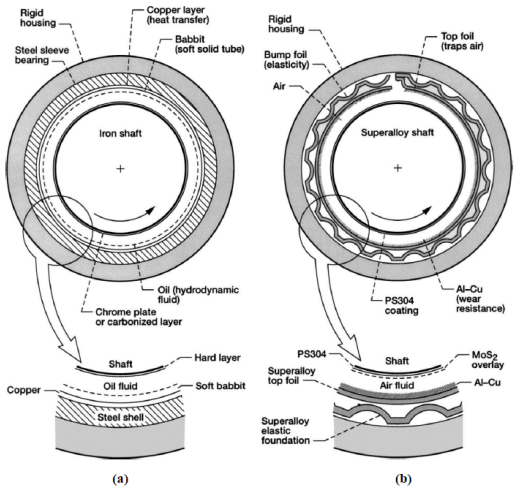

FIGURE 1.1: Schematic representation of (a) oil-film bearings and (b) foil bearings

In multiple overleaf GFBs, the compliance to flexural strain from staggered structural foils and the Coulomb friction at the contact area define their operational characteristics [7]. In corrugated bump GFBs, bump-strip layers supporting a top foil render a tunable bearing nonlinear stiffness. In this case, Coulomb friction effects arising between the bump layers and the top foil as well as the bumps and the bearing rigid shell provide the energy dissipation, thus the damping characteristics [8, 9].

First generation foil bearings, shown in Fig. 1.2 are composed of a rigid housing, a simple elastic foundation or bump foil with uniform stiffness, and the top foil and are used almost exclusively in air-cycle machines [10]. The load capacity achieved by those bearings is equal to rigid gas bearings. Second generation foil bearings display a more complex structure as the bump foil is adjusted appropriately in one direction, in order to encounter phenomena like shaft misalignment, their load capacity is approximately twice that of first generation GFBs and are used in turbocompressors and microturbines [11]. A second generation gas foil bearing is shown in Fig. 1.2. Third generation GFBs display a even more complex structure, as the bump foil is adjusted in two directions and their load capacity is almost twice that of second generation. They are used mainly in aircraft engines [11] and can be seen in Fig. 1.3. The load capacity of GFBs of each generation is displayed in Fig. 1.3.

In general, GFBs exhibit great advantages. They can be used in a wide range of temperatures, approximately from $-196^{\circ}C$ up to $650^{\circ}C$ [12]. Also, as stated above, there is no need for external pressurization. Their adaptability to various operational conditions due to foil deformation is remarkable, as well as their reliability. However, solid lubrication, to prevent power loss at low rotating speeds, is necessary [12].

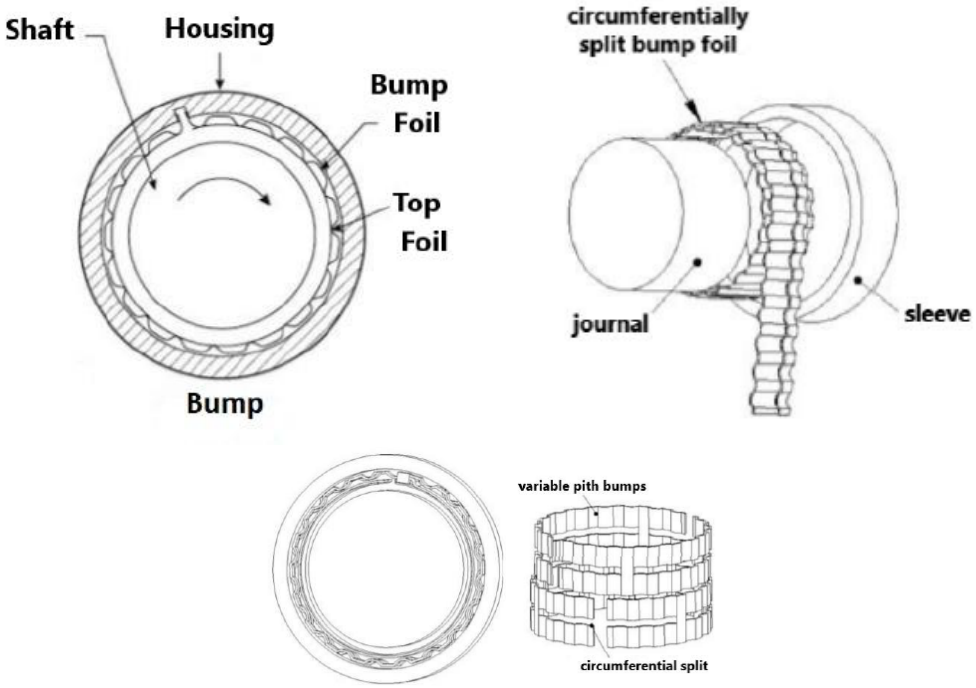

FIGURE 1.2: Gen. I, II and III GFBs [11]

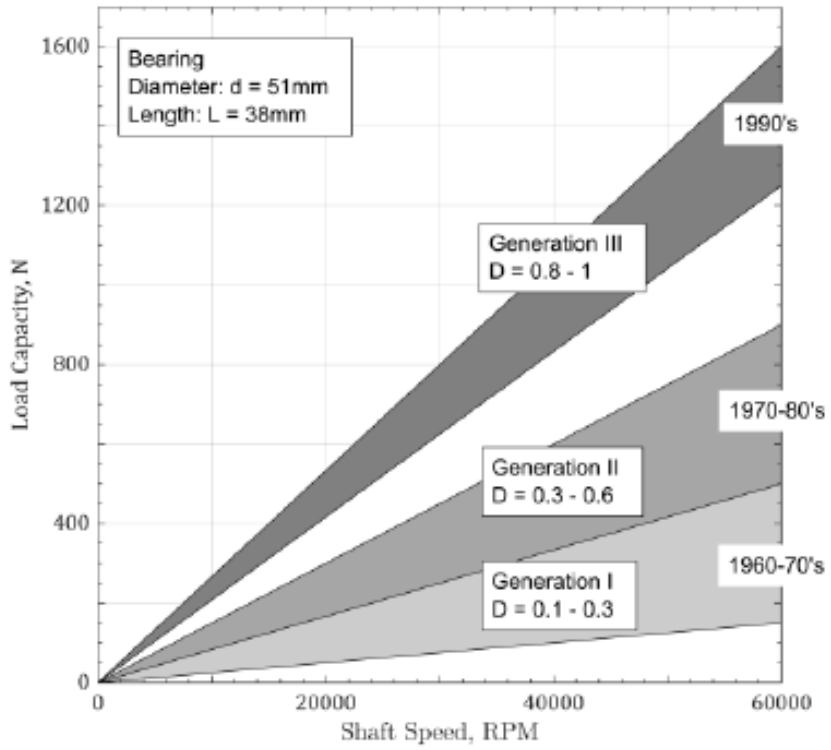

FIGURE 1.3: Load capacity of each generation [11]

1.2 Active Gas Foil Bearings

The need for controllable bearings arises from the requirement to improve the dynamic characteristics of the supported machinery, such as the suppression of the oscillation amplitudes and the elimination of instabilities within the operation range [13]. Also the necessity for adaptability to different operational conditions, such as temperature or unbalance conditions led to a mass research in this direction.

Until today, the research on active bearings mainly concerns electromagnetic bearings. Electromagnetic bearings are the only type of bearings that operate in vacuum. A conventional active magnetic bearing (AMB) system is shown in Fig. 1.4. It consists of a rotor supported by a number of Active Magnetic Bearings (AMBs), a backup rolling bearing, a thrust magnetic bearing, the electromagnetic actuators, the position sensors, the Magnetic Bearing Controller (MBC) and the cables that connect the MBC to the AMB. The position of the rotor inside the AMB is measured by the position sensors and then it is received as feedback by the controller. Then, based on the feedback control law designed by the user, the MBC produces a control signal that is sent to the AMBs, completing the closed loop system.

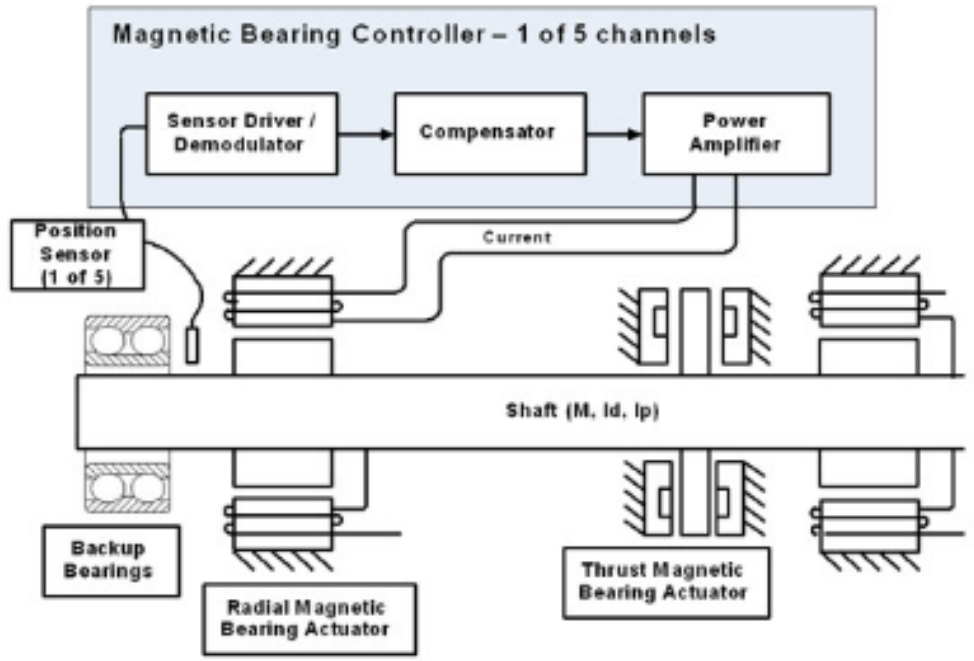

FIGURE 1.4: Classic AMB system

The most popular controller in systems supported by magnetic bearings is the PID controller [14]. T. K. Psonis et al. showed the need for a controller in order to stabilize an unstable system and chose a PID one [15]. The block diagram of the closed loop system is shown in Fig. 1.5. Furthermore, a band-limited white noise is considered in order to investigate the robustness of the closed loop system. Also, nonlinear control techniques have been used, utilizing feedback linearization and back-stepping concepts in order to achieve position and tracking control, as thoroughly explained by John Y. Hung [16].

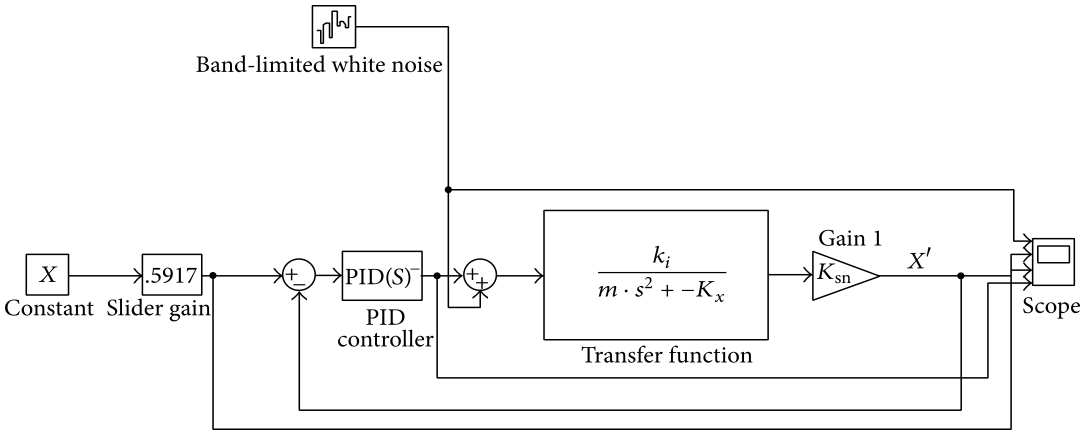

FIGURE 1.5: Closed loop system of a linearized magnetic bearing model utilizing a PID controller [15]

Apart from the magnetic bearings, a significant effort has also been made for the design and development of controllable or active GFBs. The most frequently used method is the placement of piezoelectric actuators in the circumferential direction of

the bearing, between the top foil and the rigid shell. J. Park and K. Sim proposed a active gas foil bearing (AGFB) with a laminated top foil , a classic bump foil and piezo stacks aiming to accommodate the clearance by adjusting the thickness of the piezo stacks and to mechanically preload the bearing by changing the thickness of several piezo stacks [17]. It has been found that the clearance control has a positive impact on the dynamic force coefficients of the system, whereas the preload control has a slight one. On the other hand, large preload results in a more stable passage through the critical speeds. The schematic representation of this system is illustrated in Fig. 1.6. Additionally, L. Savin et al. explain in detail the most common controllable bearing system, as shown in Fig. 1.7 [18].

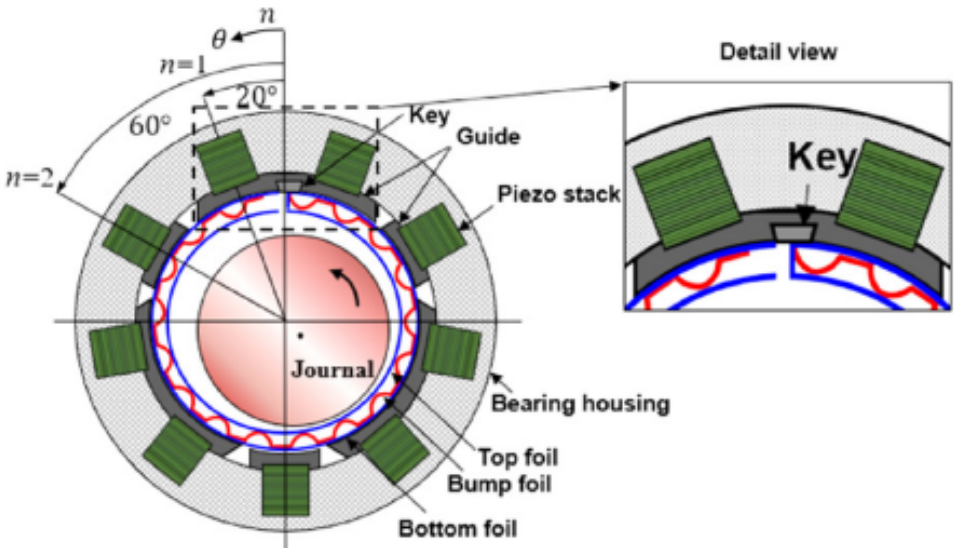

FIGURE 1.6: Schematic representation of a AGFB with piezo stacks [17]

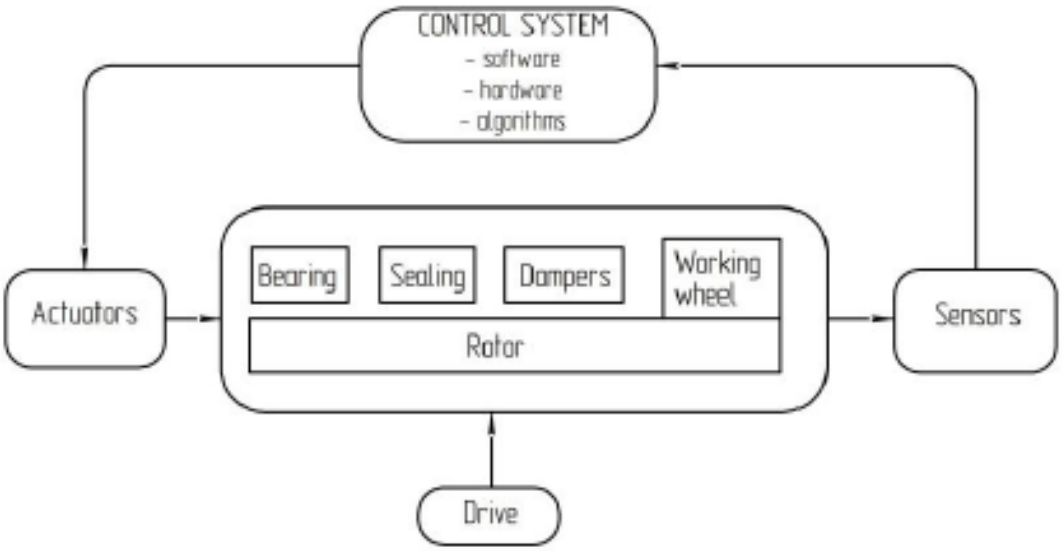

FIGURE 1.7: Common bearing control system [18]

Further, controllable GFBs with active bump foil with piezoelectric actuators were thoroughly described by K. Feng et al. [19] and GFBs with radial air injection were introduced by S. von Osmanski and I. F. Santos [20].

1.3 Current Work - Object of Study

In this work, a active gas foil bearing is considered. The bearing consists of a rigid shell (bearing sleeve), a thin top foil and piezoelectric actuators allowed to move radially. The bump foil is absent and the actuators are connected to the top foil by springs, which are considered to be linear with stable stiffness. The model of the bearing, along with the resulting gas forces acting on the top foil and on the rotor, are shown in Fig. 1.8. The system is composed of 2 identical AGFBs , a rigid rotor with a disc located in its center, as shown in Fig 1.9.

In Chapter 2 the modeling of the system is presented. The top foil is modeled using a Finite Element Method and the resulting matrices are reduced using the Guyan Reduction Method [21]. The Reynolds equation governing compressible fluid lubrication [22] is discretized with Central Finite Differences. The differential equations concerning the rotor are derived by the Lagrangian Method. At the end of Chapter 2, simulation results are presented for bearings with different nominal top foil diameters, with different ways of placing the actuators and with different values of the disc mass. In Chapter 3 a Linear Control Method using an observer is used in order to stabilize unstable fixed points of the balanced system, namely zero unbalance grade. Also, a polynomial feedback control law is used in order to eliminate Hopf Bifurcations of the balanced system. The same feedback law is used to suppress the oscillation amplitudes and produce output synchronous signals. Furthermore, a design optimization procedure to locate the fixed point of the balanced system in a desired location is presented.

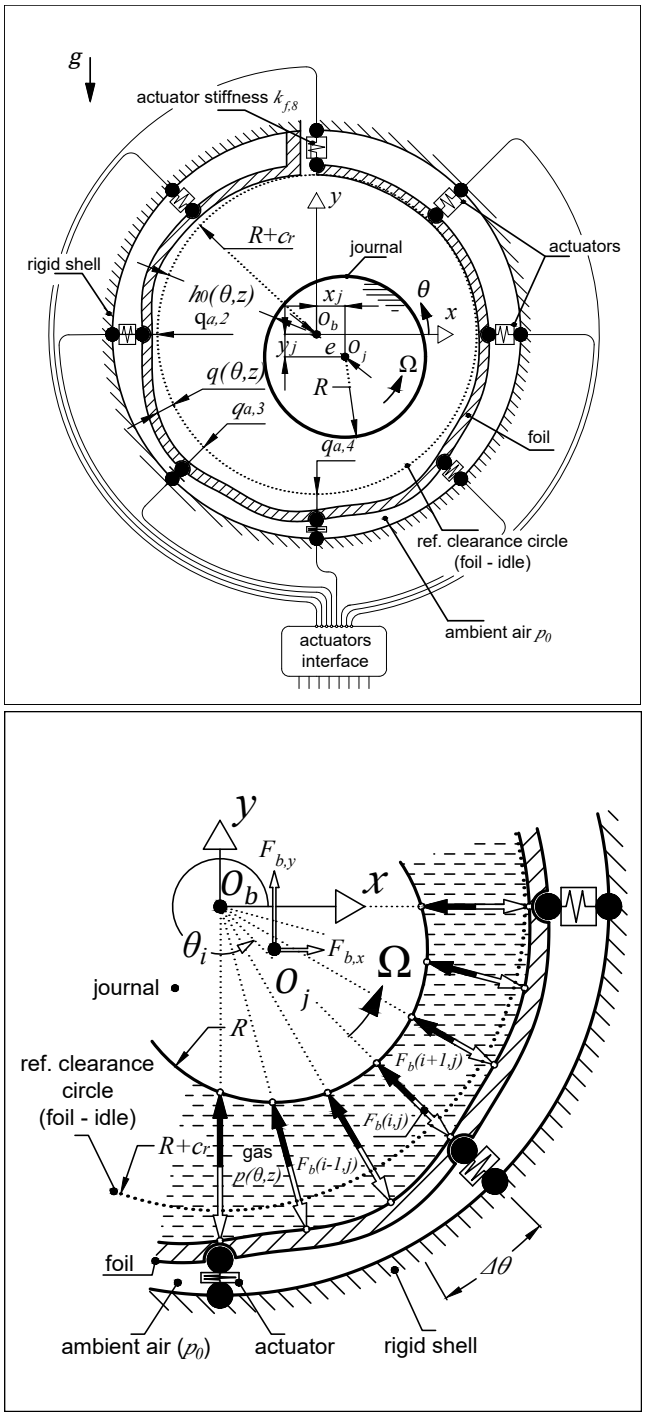

FIGURE 1.8: AGFB model and resulting gas forces

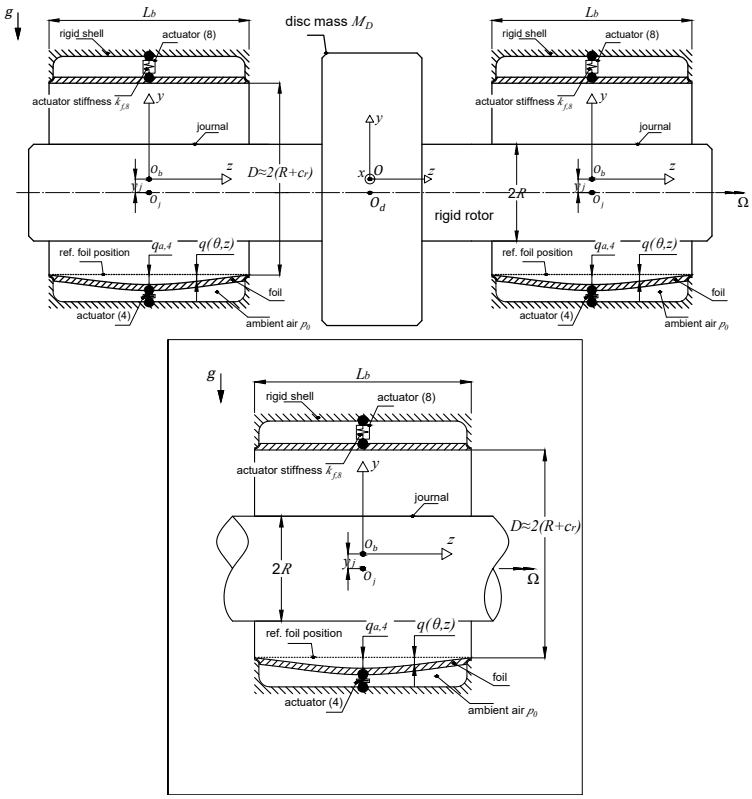

FIGURE 1.9: Front and side view of the rigid shaft with a mass disc supported by 2 identical AGFBs

Chapter 2

Modelling and Composition of the Dynamical System

In this chapter, the modeling of the dynamical system is thoroughly presented and explained. Initially, the foil is assumed to behave as a thin flat plate and the equations of motion are derived using the MZC finite element [23, 24] followed by the static Guyan Reduction [21]. The piezoelectric actuators are added and then, the motion equations are converted into state equations. A semi-discrete approach is then used in order to reduce the Reynolds Equation, which is a Partial Differential Equation, to a system of Ordinary Differential Equations, i.e the state equations that govern the pressure field [25]. The Lagrangian Method [26] is used in order to derive the equations of motion of the rotor and, consequently, the state equations. The resulting full system is nonlinear and the results of simulations for different bearing geometries and actuator placement are extracted. For the implementation of the thesis the Matlab programming language was exclusively used [27].

2.1 Modelling of the Active Gas Foil Bearing

In actual GFBs the foil is a thin shell. A shell, in general, is considered as the superposition of plane stress and bending [28]. In this work, the plane stress is ignored, as the corresponding deformations are small in relation to the vertical deformation, therefore the foil is supposed to be a bending thin plate. After the discretization of the foil and the construction of the FE mesh, each node is allowed to be displaced perpendicular to the mid-surface of the plate. Those deflections are considered as the radial displacements of the foil. Also, each node is allowed to perform two rotations around the two axes that are perpendicular to the normal vector of the plate surface. Later, those rotations will be eliminated using the Guyan Reduction mentioned above.

2.1.1 Computational Model of the Deformable Foil

After extensive research in the literature, the foil modelling effort started using the quadratic isoparametric plate bending element PBL4 [24]. In order to cover the case of thin plates, a 2x2 Gauss Quadrature integration used to calculate the bending contribution to the stiffness matrix and 1x1 Gauss Quadrature integration to calculate the shear one [29]. It was noticed that due to the small thickness, there was the phenomenon of shear locking which was undesirable. Shear lock is a phenomenon where a artificial shear is introduced to the model. This happens mainly because of the linear nature of the element, as the shape functions of this element are first order polynomials. As a result, the structure appears to be much more stiffer than

it actually is and the elements reach equilibrium with smaller displacements, so a numerical error occurs. Shear lock is easy to detect, as the numerical error is accompanied by a visual error, as ripples on the surface of the plate are noticed. To eliminate this phenomenon, one should increase the thickness of the plate. In the case of the top foil modelling this was not desirable. Finally, it was decided to use another element that does not take into account the shear contribution to the stiffness matrix, the MZC plate bending element. That element was designed to be applicable to thin plates exclusively. Analytical integration for the calculation of the element matrices was used and a sensitivity analysis for the selection of the number of elements followed.

The top foil is divided into a mesh of thin rectangular elements. A MZC element is shown in Fig. 2.1

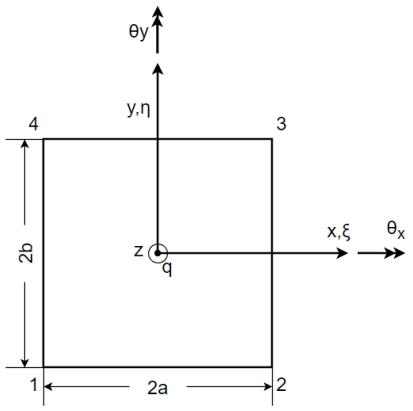

FIGURE 2.1: MZC plate bending element

The side parallel to the x-axis has a length of $2a$ and the side parallel to the y-axis has a length of $2b$. It is important to note that these axes are the local axes of the element and the origin of the local coordinate system is located in the center of the element. Each element consists of four nodes with three degrees of freedom at each node, therefore each element has twelve degrees of freedom. These degrees of freedom are the displacements normal to the plane of the element q_i, the rotations around x-axis, $\theta_{x_i} = \frac{\partial q_i}{\partial y}$, and the rotations around y-axis, $\theta_{y_i} = -\frac{\partial q_i}{\partial x}$, $i = 1, ..., 4$. Then, the dimensionless local coordinates $\xi = \frac{x}{a}$ and $\eta = \frac{y}{b}$ are introduced. The vector of DOFs of each element is

$$\mathbf{w_e} = \left\{q_1 \ \theta_{x_1} \ \theta_{y_1} \ q_2 \ \theta_{x_2} \ \theta_{y_2} \ q_3 \ \theta_{x_3} \ \theta_{y_3} \ q_4 \ \theta_{x_4} \ \theta_{y_4}\right\}^T \tag{2.1}$$

The vertical displacement of a point in the interior of the element is approximately calculated by the equation

$$w(\xi, \eta) = \left\{\mathbf{N_1} \ \mathbf{N_2} \ \mathbf{N_3} \ \mathbf{N_4}\right\} \cdot \mathbf{w_e} = \mathbf{N} \cdot \mathbf{w_e} \tag{2.2}$$

where

$$\mathbf{N_i}(\xi, \eta) = \left\{ \begin{array}{c} \frac{1}{8}\left(1+\xi_i\xi\right)\left(1+\eta_i\eta\right)\left(2+\xi_i\xi+\eta_i\eta-\xi^2-\eta^2\right) \\ \frac{b}{8}\left(1+\xi_i\xi\right)\left(\eta_i+\eta\right)\left(\eta^2-1\right) \\ -\frac{a}{8}\left(\xi_i+\xi\right)\left(\xi^2-1\right)\left(1+\eta_i\eta\right) \end{array} \right\}^T \tag{2.3}$$

is the vector of shape functions of the DOFs corresponding to the node i and ξ_i, η_i are the dimensionless coordinates of the node i. These dimensionless coordinates of the nodes $i = 1, ...4$ are shown in table 2.1.

node i	1	2	3	4
ξ_i	-1	1	1	-1
η_i	-1	-1	1	1

TABLE 2.1: Dimensionless coordinates of nodes $i = 1, ..., 4$

Also, the following matrices are introduced

$$\mathbf{B_s} = \begin{Bmatrix} \frac{\partial^2}{\partial x^2} \\ \frac{\partial^2}{\partial y^2} \\ 2\frac{\partial^2}{\partial x \partial y} \end{Bmatrix} \cdot \mathbf{N}(x,y) = \begin{Bmatrix} \frac{1}{a^2}\frac{\partial^2}{\partial \xi^2} \\ \frac{1}{b^2}\frac{\partial^2}{\partial \eta^2} \\ \frac{2}{ab}\frac{\partial^2}{\partial \xi \partial \eta} \end{Bmatrix} \cdot \mathbf{N}(\xi,\eta) \tag{2.4}$$

and

$$\mathbf{D} = \begin{bmatrix} \frac{E}{1-v^2} & \frac{Ev}{1-v^2} & 0 \\ \frac{Ev}{1-v^2} & \frac{E}{1-v^2} & 0 \\ 0 & 0 & G \end{bmatrix} \tag{2.5}$$

where $\mathbf{B}$ is the strain matrix, $\mathbf{D}$ is the material matrix, E is the Young's modulus, G is the shear modulus and v is the Poisson ratio. The material of the foil is considered to be steel and its properties are shown in table 2.2.

$E(N/mm^2)$	210000
$\rho(kg/m^3)$	7860
v	0.3

TABLE 2.2: Top foil material properties

The element stiffness matrix is

$$\mathbf{K_e} = \int_{-b}^{b}\int_{-a}^{a} \frac{h_f^3}{12}\, \mathbf{B_s}^T \cdot \mathbf{D} \cdot \mathbf{B_s}\, dxdy = \int_{-1}^{1}\int_{-1}^{1} \frac{abh_f^3}{12}\, \mathbf{B_s}^T \cdot \mathbf{D} \cdot \mathbf{B_s}\, d\xi d\eta \tag{2.6}$$

and the element mass matrix is

$$\mathbf{M_e} = \int_{-b}^{b}\int_{-a}^{a} \rho h_f\, \mathbf{N}^T \cdot \mathbf{N}\, dxdy = \int_{-1}^{1}\int_{-1}^{1} ab\rho h_f\, \mathbf{N}^T \cdot \mathbf{N}\, d\xi d\eta \tag{2.7}$$

where h_f is the thickness of the top foil and ρ is the density of the material of the top foil. The element force vector is calculated from the equation

$$\mathbf{F_e} = \int_{-b}^{b}\int_{-a}^{a} \mathbf{N}^T p(x,y) dxdy = \int_{-1}^{1}\int_{-1}^{1} ab\mathbf{N}^T p(\xi,\eta) d\xi d\eta \tag{2.8}$$

where $p(x,y)$ is a distributed load over the surface of the foil. Then, the global stiffness $\mathbf{K}$ and mass $\mathbf{M}$ matrices and the global force vector $\mathbf{F}$ are constructed. Also,

a damping matrix is introduced to the system. This damping matrix is calculated as

$$\mathbf{C} = \eta_f \mathbf{K} \tag{2.9}$$

where η_f is the Rayleigh damping factor of the foil. As a result, the foil motion equations are

$$\mathbf{M} \cdot \ddot{\mathbf{w}} + \mathbf{C} \cdot \dot{\mathbf{w}} + \mathbf{K} \cdot \mathbf{w} = \mathbf{F} \tag{2.10}$$

where $\mathbf{w}$ is a vector containing the DOFs of the foil and $\mathbf{F}$ is the vector of gas forces acting on the foil. Concluding, the Guyan Reduction Method is used and the reduced motion equations of the top foil are

$$\mathbf{M_r} \cdot \ddot{\mathbf{q}} + \mathbf{C_r} \cdot \dot{\mathbf{q}} + \mathbf{K_r} \cdot \mathbf{q} = \mathbf{F_r} \tag{2.11}$$

The vector $\mathbf{q}$ contains only the radial displacements of the FE mesh nodes and $\mathbf{M_r}$, $\mathbf{C_r}$, $\mathbf{K_r}$, $\mathbf{F_r}$ are the corresponding reduced mass, damping, stiffness matrices and force vector accordingly. The application of Guyan Reduction introduces a minimal error, but decreases the computational cost to a significant extent. This method is presented in Appendix A. Furthermore, the calculation of the components of the force vector is achieved by using Gauss - Lobatto Quadrature [30]. It is important to note that the FE mesh global coordinate system concerns only the foil. The foil folds in such a way that the displacement of a node is considered positive when that node moves radially outwards. Similarly, an external force is considered positive if it points radially outwards and negative if it points radially inwards.

Two different bearing geometries are considered. In both cases the foil length to foil diameter ratio is $L_f/D_f = 1$. The foil FE mesh consists of sixteen elements in the x-direction and ten elements in the y-direction and is shown in Fig. 2.2. The perimeter of the foil is πD_f. The right edge of the top foil is clamped, therefore the deflections and rotations corresponding to those nodes are all zero. The other three edges are free. The first bearing has a diameter of 30 mm and will be referred as Bearing D30. The second bearing has a diameter of 100 mm and will be referred as Bearing D100. The clearance of each bearing is $c_r = \frac{D_f}{1000}$. Two bearing diameters are tested in order to validate the following results for a high speed system (D30, operating at $\Omega < 200\,kRPM$), and a medium speed system (D100, operating at $\Omega < 65\,kRPM$). Tangential velocity of both journals reach the speed of sound when rotating speed is at its maximum. Therefore, both bearings are characterized as DN = 6.500.000 bearings, where DN = Diameter[mm] times N[RPM]. This value characterizes a system as an ultra-high speed system.

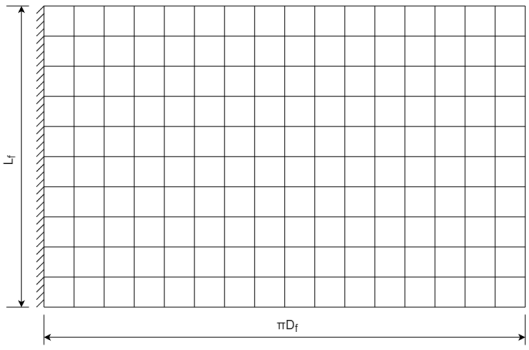

FIGURE 2.2: Finite element mesh of the foil with sixteen elements in the circumferential direction and ten elements in the axial direction. The elements have the same aspect ratio.

2.1.2 Implementation of piezoelectric (PZT) actuators

For the actual displacement of the foil, piezoelectric actuators are considered as one solution in this thesis. Piezoelectric actuators are elements used in applications that require precise movement of an embedded element. No moving parts, e.g. gears, are included. Their displacement is a result of the ability of the material from which they are made to expand or contract when a voltage is applied to it. The materials that are usually used are ceramics and specifically lead zirconate titanate (PZT), barium titanate and lead titanate. In this thesis, a simple model of a massless longitudinal piezoelectric actuator is considered. Each actuator is connected to the foil and the rigid shell via simple supports (hinged supports). A representative value for the stiffness of each actuator is taken into account in the foil support model. The displacement of each actuator is defined as the radial displacement of the hinged support at the rigid shell (outer shell), see Fig. 1.8.The linear stiffness of the actuator is defined as k_f. A representation of this model is shown in Fig. 1.8. The expansion or contraction of the linear spring depends exclusively on its compliance and on the displacement of its two ends, while the displacement of the actuator is determined by the user and is denoted by q_a, see Fig. 1.8. The displacement of the longitudinal actuator in the radial direction is

$$\delta L = n d_{33} V \tag{2.12}$$

where n is the number of stacked layers, d is a deformation coefficient measured in m/V and V is the voltage input measured in V. In this work, its is considered $d_{33} = 0.003 m/V$ and $n = 25$.

Assuming that the actuator j is connected to the node i of the top foil discretized domain, the additional force on this node will be equal to $F_{act_{ij}} = k_{f_i}(q_{a_j} - q_i)$. Therefore, eq. 2.11 become

$$\begin{aligned} \mathbf{M_r} \cdot \ddot{\mathbf{q}} + \mathbf{C_r} \cdot \dot{\mathbf{q}} + \mathbf{K_r} \cdot \mathbf{q} &= \mathbf{F_r} + \mathbf{F_{act}} \\ \mathbf{M_r} \cdot \ddot{\mathbf{q}} + \mathbf{C_r} \cdot \dot{\mathbf{q}} + \mathbf{K_r} \cdot \mathbf{q} &= \mathbf{F_{tot}} \end{aligned} \tag{2.13}$$

where $\mathbf{F_{act}}$ is a vector containing the forces due to the displacements of the actuators and has that many nonzero components, as the number of actuators. Similarly to the foil displacements, the displacements of the actuators are considered positive when

they move radially outwards. Concluding, the state equations of the foil are

$$\frac{d}{dt}\begin{Bmatrix}\mathbf{q}\\ \dot{\mathbf{q}}\end{Bmatrix} = \begin{bmatrix}\mathbf{O} & \mathbf{I}\\ -\mathbf{M_r}^{-1}\cdot\mathbf{K_r} & -\mathbf{M_r}^{-1}\cdot\mathbf{C_r}\end{bmatrix}\cdot\begin{Bmatrix}\mathbf{q}\\ \dot{\mathbf{q}}\end{Bmatrix} + \begin{Bmatrix}\mathbf{O}\\ \mathbf{M_r}^{-1}\cdot\mathbf{F_{tot}}\end{Bmatrix} \tag{2.14}$$

Consequently, the foil state equations can be written in the form

$$\frac{d}{dt}\begin{Bmatrix}\mathbf{q}\\ \dot{\mathbf{q}}\end{Bmatrix} = \mathbf{f_f}\left(\mathbf{q}, \dot{\mathbf{q}}, \mathbf{p}; \mathbf{q_a}\right) \tag{2.15}$$

where $\mathbf{q_a}$ is a vector with components the displacements of the actuators.

2.2 Solution of the Aerodynamic Lubrication Problem

Gas foil bearings use atmospheric air at ambient pressure to form a lubricating film. Between the smooth top foil and the outer surface of the shaft the phenomenon of aerodynamic lubrication appears. The longitudinal axes of the bearing and the shaft are parallel, therefore no angular misalignment is considered. The geometrical center of the bearing is denoted by O_b, while the geometrical center of the cross section of the shaft is denoted by $O_j\left(x_j, y_j\right)$. The distance between those centers is called journal eccentricity and is calculated as $e = \sqrt{x_j^2 + y_j^2}$. The foil deformation, $q_i\left(t, \theta, z\right)$, as mentioned earlier, is a result of the pressure and the displacements of the actuators. The angle coordinate θ is measured from the positive x semi-axis. At $\theta = \frac{\pi}{2}$ the top foil is clamped and its deformation and velocity are zero. These are shown in Fig. 1.8.
The Reynolds equation governing the phenomenon of compressible fluid lubrication is derived, taking into account the following assumptions [25]:

- The gas film is isothermal, namely the temperature is constant and independent of pressure
- The flow is laminar
- At the solid boundary and flow field interface the solid-fluid relative velocities are zero
- The fluid inertia is negligible
- The fluid is ideal, i.e $\frac{p}{\rho_{air}} = ct$
- There are no fluid leaks
- $R_f = R + c_r \approx R$, where R is the radius of the rotor and c_r is the clearance
- The pressure does not change in the radial direction of the bearing

Under those assumptions, the Reynolds equation describing the pressure field is

$$\frac{\partial}{\partial\chi}\left(ph^3\frac{\partial p}{\partial\chi}\right) + \frac{\partial}{\partial z}\left(ph^3\frac{\partial p}{\partial z}\right) = 6\mu R\Omega\frac{\partial}{\partial\chi}\left(ph\right) + 12\mu\frac{\partial}{\partial t}\left(ph\right) \tag{2.16}$$

or

$$\dot{p} = \frac{h^2}{12\mu}\left(p_\chi^2 + p_z^2\right) + \frac{ph}{4\mu}\left(h_\chi p_\chi + h_z p_z\right) + \frac{ph^2}{12\mu}\left(p_{\chi\chi} + p_{zz}\right) - \frac{R\Omega}{2}p_\chi - \frac{R\Omega p}{2h}h_\chi - \frac{p}{h}\dot{h} \tag{2.17}$$

where p is the fluid pressure, h is the fluid film thickness, μ is the dynamic viscosity of the air and Ω is the rotational speed of the rotor. Eq. 2.17 is a nonlinear partial differential equation and does not have closed form analytical solution. Therefore, it is solved numerically using a semi-discrete approach with central finite differences [25]. In Eq. 2.16 and 2.17 it is considered that $\frac{\partial \chi}{\partial \theta} = R$. The grid that is used in order to solve the equation 2.17 consists of sixteen intervals in the χ-direction, therefore, $N\chi = 16$ and $Nz = 10$ intervals are defined in the Finite Difference grid for the Reynolds equation. The thickness of the gas film, as a function of θ and z is

$$\begin{aligned} h\left(t,\theta,z\right) &= c_r - x_j\left(t\right)cos\theta - y_j\left(t\right)sin\theta + q\left(t,\theta,z\right) \\ h_{pq}\left(t\right) &= c_r - x_j\left(t\right)cos\theta_p - y_j\left(t\right)sin\theta_{+}q_{pq}\left(t\right) \end{aligned} \tag{2.18}$$

The boundary conditions required for the solution of Eq. 2.17 are

$$\begin{aligned} p\left(t,0,z\right) = p\left(t,2\pi,z\right) = p_0 \Rightarrow p_{1,j}\left(t\right) = p_{N_\chi+1,j}\left(t\right) = p_0 \\ p\left(t,\theta,0\right) = p\left(t,\theta,L_f\right) = p_0 \Rightarrow p_{i,1}\left(t\right) = p_{i,N_z+1}\left(t\right) = p_0 \end{aligned} \tag{2.19}$$

and the initial condition is

$$p\left(0,\theta,z\right) = p_0 \tag{2.20}$$

where p_0 is the ambient pressure. It is important to note that because of the semi-discrete approach, the pressures $p_{i,j}$ are functions of time t, but the dependence on time is implicit.

Concluding, the state equations of the pressure field are

$$\dot{\mathbf{p}} = \mathbf{f_p}\left(\mathbf{q},\dot{\mathbf{q}},\mathbf{p},\mathbf{x_j},\dot{\mathbf{x}}_\mathbf{j};\Omega\right) \tag{2.21}$$

In Eq. 2.21, $\mathbf{x_j} = \left\{x_j\ \dot{x}_j\ \ y_j\ \dot{y}_j\right\}^T$ is the vector containing the DOFs of the rotor.

The gas forces acting on the rotor are calculated as

$$\begin{aligned} F_{B_x} &= -\int_0^{2\pi}\int_0^{L_f}\left(p-p_0\right)cos\theta = -\sum_{i=2}^{N_\chi}\sum_{j=2}^{N_z}\left(p_{i,j}-p_0\right)cos\theta_i\Delta\chi\Delta z \\ F_{B_y} &= -\int_0^{2\pi}\int_0^{L_f}\left(p-p_0\right)sin\theta = -\sum_{i=2}^{N_\chi}\sum_{j=2}^{N_z}\left(p_{i,j}-p_0\right)sin\theta_i\Delta\chi\Delta z \end{aligned} \tag{2.22}$$

It is common that sup-ambient pressures arise in the bearing. In such cases, when calculating the resulting gas forces on the rotor or on the top foil, those sub-ambient pressures are considered to be ambient, according to Heshmat et al.

2.3 Rigid Rotor on Active Gas Foil Bearings

Apart from the rotation, the rotor has two more DOFs, the x-displacement and the y-displacement. Those displacements are results of the forces acting on the rotor. Those forces are of three types:

- Gas forces, calculated from Eq. 2.22,
- Gravity forces, depending on the mass of the disc and

- Unbalance forces

Unbalance forces are centrifugal forces appearing on the rotor due to the non-uniformly distributed mass of the disc and the rotational speed. This leads to vibrations that, often, need to be suppressed. The unbalance force in the x-direction is denoted by F_{U_x} and in the y-direction by F_{U_y}. If the rotational speed is constant, these unbalance forces are

$$F_{U_x} = m_d e_u \Omega^2 cos\left(\phi_r\right), \; F_{U_y} = m_d e_u \Omega^2 sin\left(\phi_r\right) \tag{2.23}$$

where $\phi_r = \Omega t$ and m_d is the mass of the disc. If the rotational speed is linearly dependent on time, namely $\Omega = \alpha t$, with α representing the rotational acceleration, the unbalance forces are

$$F_{U_x} = m_d e_u \left(\Omega^2 cos\phi_r + \alpha sin\phi_r\right), \; F_{U_y} = m_d e_u \left(\Omega^2 sin\phi_r - \alpha cos\phi_r\right) \tag{2.24}$$

where $\phi_r = \alpha t^2/2$. The unbalance eccentricity e_u is calculated according to the ISO unbalance grades, known as G-grades. In this work medium (G2.5) and high (G6.3) unbalance grades will be considered. The disc unbalance is of magnitude $u = m_d e_u$ and the eccentricity is

$$e_u[m] = 0.001 \frac{G}{\Omega_r}, \;\; G = 2.5, 6.3 \tag{2.25}$$

where Ω_r is the maximum service speed. The motion equations of the rotor are then derived using the Lagrangian Method.

$$\ddot{x}_j = \frac{F_{B_x}}{m_d} + \frac{F_{U_x}}{md}, \; \ddot{y}_j = \frac{F_{B_y}}{m_d} + \frac{F_{U_y}}{md} - g \tag{2.26}$$

where g is the gravitational acceleration. Therefore, the state equations of the rotor are

$$\dot{x}_1 = x_2, \;\; \dot{x}_2 = \frac{F_{B_x}}{m_d} + \frac{F_{U_x}}{md}, \;\; \dot{x}_3 = x_4, \;\; \dot{x}_4 = \frac{F_{B_y}}{m_d} + \frac{F_{U_y}}{md} - g \tag{2.27}$$

or

$$\dot{\mathbf{x}}_\mathbf{j} = \mathbf{f}_\mathbf{R}\left(t, \mathbf{p}, \mathbf{x}_\mathbf{j}, \dot{\mathbf{x}}_\mathbf{j}; \Omega\right) \tag{2.28}$$

where $x_1 = x_j$, $x_2 = \dot{x}_j$, $x_3 = y_j$ and $x_4 = \dot{y}_j$.

2.4 Full Nonlinear Dynamical System

The $N = 491$ state variables of the full system are derived from Eq. 2.15, 2.21, 2.28 and are gathered in the state vector

$$\mathbf{x} = \left\{\mathbf{p} \;\; \mathbf{q} \;\; \dot{\mathbf{q}} \;\; \mathbf{x_j} \;\; \dot{\mathbf{x}}_\mathbf{j}\right\}^T \tag{2.29}$$

Therefore, the system of ODEs representing the coupled nonlinear system is

$$\dot{\mathbf{x}} = \mathbf{f}\left(t, \mathbf{p}, \mathbf{q}, \dot{\mathbf{q}}, \mathbf{x_j}, \dot{\mathbf{x}}_\mathbf{j}; \mathbf{q_a}, \Omega\right) = \mathbf{f}\left(t, \mathbf{x}; \mathbf{q_a}, \Omega\right) \tag{2.30}$$

The system has a number of parameters, the M displacements of the actuators and the rotational speed Ω. The vector field $\mathbf{f}$ is a mapping from the parametric state space to the state space, i.e $\mathbf{f} : \mathbb{R}^{N+M+1} \longrightarrow \mathbb{R}^N$. In Chapter 3, the displacements of the actuators will either be considered zero, or will follow a control feedback law, therefore the system will have only one parameter, the rotational speed Ω. Note that in the case of nonzero unbalance grade, the system is non-autonomous, as the time

t appears explicitly in the state equations. Otherwise, it is a autonomous system. In the case of the balanced rotor and for fixed displacements of the actuators, the state equations are written in the form

$$\dot{\mathbf{x}} = \mathbf{f}(\mathbf{x}; \Omega) \tag{2.31}$$

Further, for each value of the rotational speed Ω, the system has been found to have a single equilibrium point $\mathbf{x}^*$, namely a point in the state space where the time derivative of the state variables becomes zero, as shown in 2.32.

$$\mathbf{f}(\mathbf{x}^*) = 0 \tag{2.32}$$

2.5 Reference Simulation Results - Open Loop System

In the last section of this chapter, several results from simulations are presented. Both bearings are investigated, for different disc masses and actuator placement. The different ways of placement of the actuators for each bearing is shown in Fig. 2.3 and 2.4. In the case of bearing D100, twenty four actuators are used and in the case of the bearing D30 twelve actuators are used. Also, two different configurations for each bearing are considered. In the first configuration, all actuators are free to move. In the second configuration, only the actuators placed in the mid plane are free to move, whereas the other will have a fixed displacement. Furthermore, in this work, the angular acceleration will be considered zero, therefore, all the results will refer to cases of rotors with constant rotational speed.

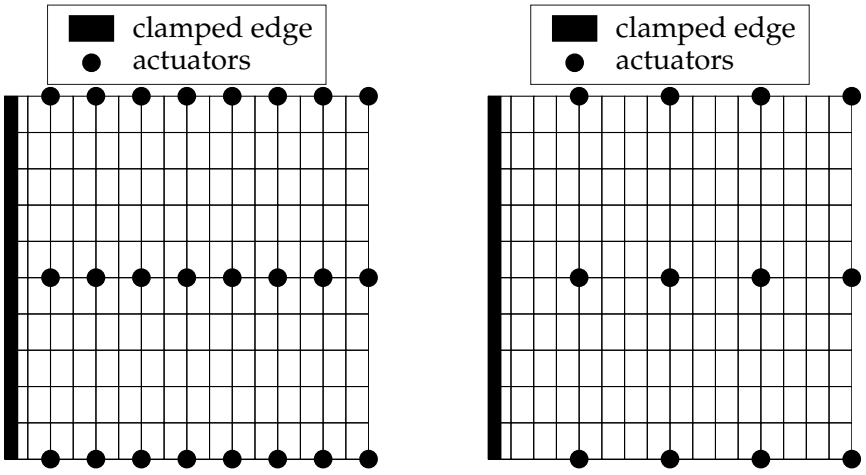

(a) Placement of the twenty four moving actuators for the bearing D100

(b) Placement of the twelve moving actuators for the bearing D30

FIGURE 2.3: First configuration of the placement of the actuators

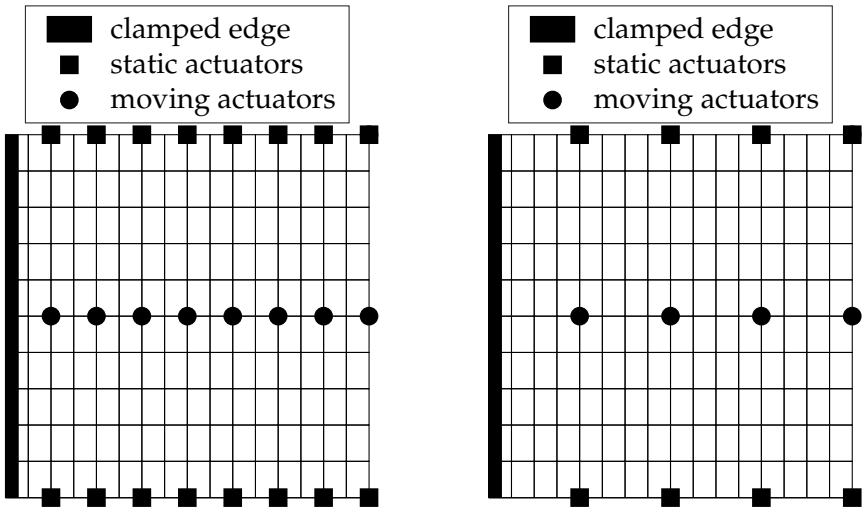

(a) Placement of the eight moving and sixteen static actuators for the bearing D100

(b) Placement of the four moving and eight static actuators for the bearing D30

FIGURE 2.4: Second configuration of the placement of the actuators

2.5.1 Results for the Bearing of Diameter D100

First, the case of the bearing D100 is presented. The thickness of the top foil is $h_f = 0.5\,mm$, the Rayleigh damping factor is $\eta_h = 0.001\,s$, the stiffness of the actuators is $k_f = 80\,\frac{N}{\mu m}$ and the displacement of the actuators is zero, $\mathbf{q_a} = \mathbf{0}$.

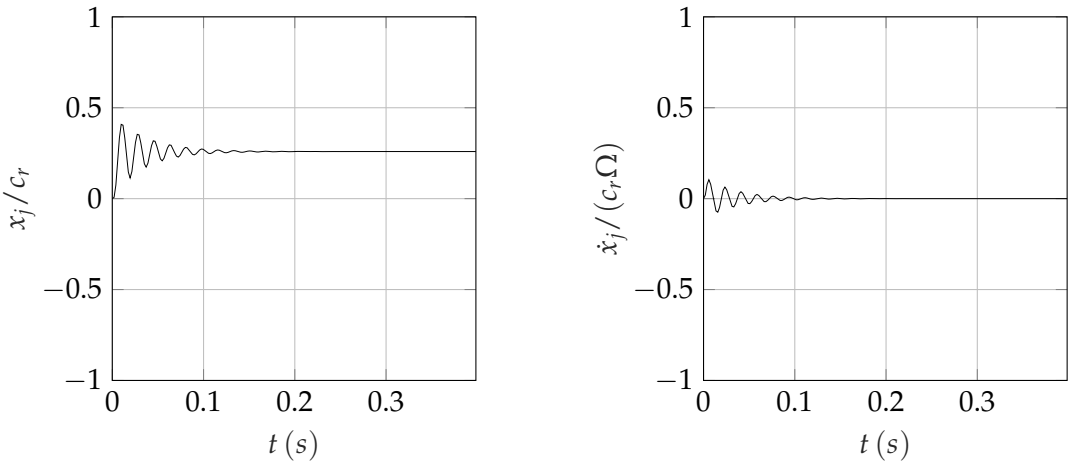

(a) x-displacement

(b) x-velocity

FIGURE 2.5: Displacement (a) and velocity (b) of the center of the disc in the x-direction at $\Omega = 700\,rad/s$. Bearing D100. Disc mass $m_d = 1\,kg$. Balanced rotor

Fig. 2.5 shows that the x-displacement of the disc reaches equilibrium state in finite time and the corresponding velocity becomes zero. In such cases, the equilibrium point of the system is said to be stable and acts as an attractor. The same is shown in Fig. 2.6 for the y-displacement and y-velocity. Also, the pressure distribution, the thickness of the lubrication film and the deformation of the foil corresponding to this equilibrium state are shown in Fig. 2.7. The orbit of the center of the disc is shown in Fig. 2.8.

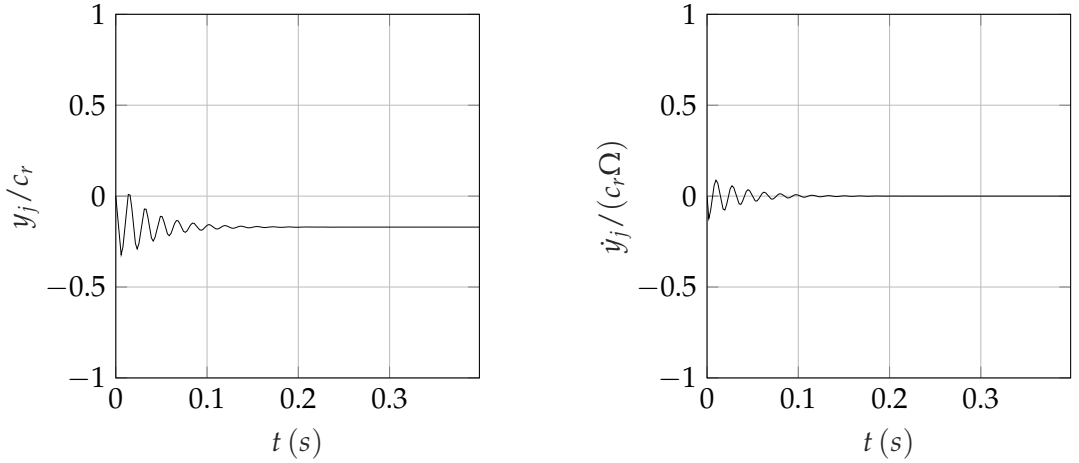

(a) y-displacement

(b) y-velocity

FIGURE 2.6: Displacement (a) and velocity (b) of the center of the disc in the y-direction at $\Omega = 700\,rad/s$. Bearing D100. Disc mass $m_d = 1\,kg$. Balanced rotor

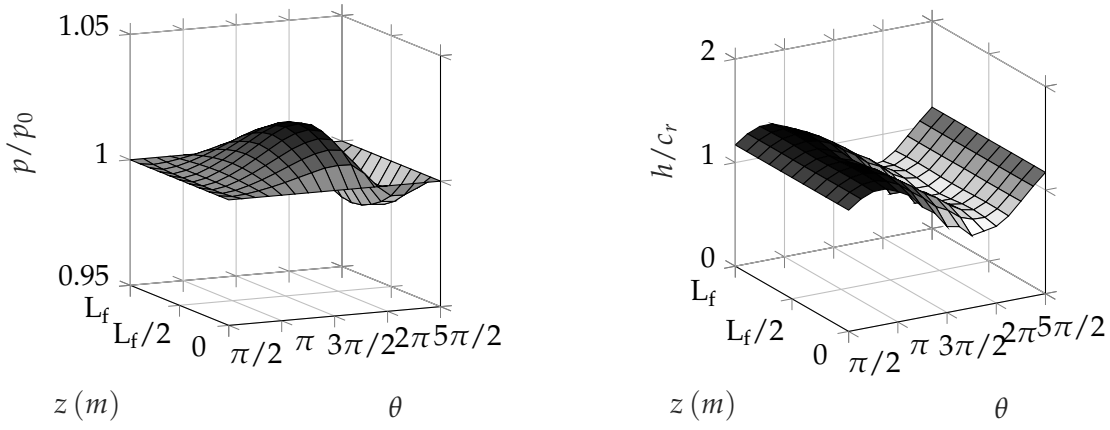

(a) pressure distribution

(b) film thickness

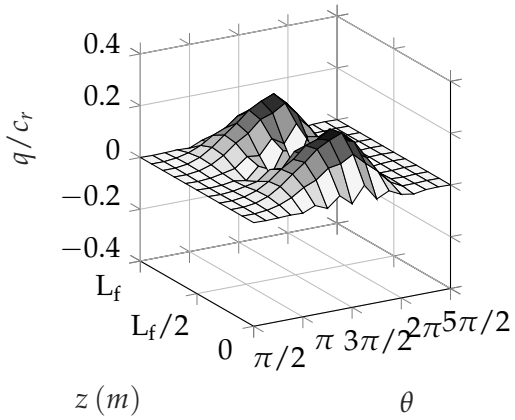

(c) foil deformation

FIGURE 2.7: Stable equilibrium pressure distribution (a), film thickness (b) and foil deformation (c) at $\Omega = 700\,rad/s$. Bearing D100. Disc mass $m_d = 1\,kg$. Balanced rotor

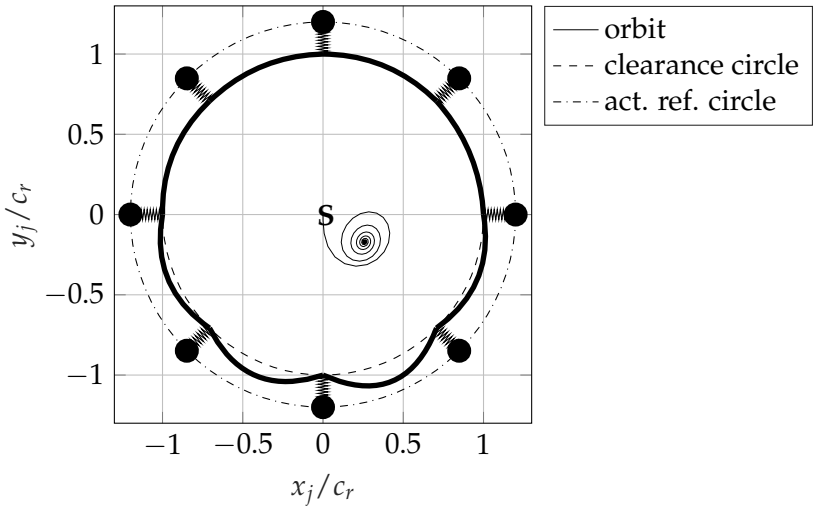

FIGURE 2.8: Orbit of the center of the disc at $\Omega = 700\,rad/s$. Bearing D100. Balanced rotor. Disc mass $m_d = 1\,kg$. The shape of the foil corresponds to the mid plane at $t = 0.4\,s$.

As the rotational speed is increased from $700\,rad/s$ to $850\,rad/s$, the disc displacements and velocities shown in Fig. 2.9, 2.10 and Fig. 2.11 do not reach fixed point equilibrium and an oscillation is observed, despite the fact that there are no external harmonic forces acting on the rotor (self-excited motion). The resulting limit cycle, shown in Fig. 2.11, is stable. Such a system, has an unstable equilibrium point. Note that in Fig. 2.8 and 2.11 (a), the value of the diameter of the actuators reference circle does not correspond to the actual value of the diameter of the rigid shell.

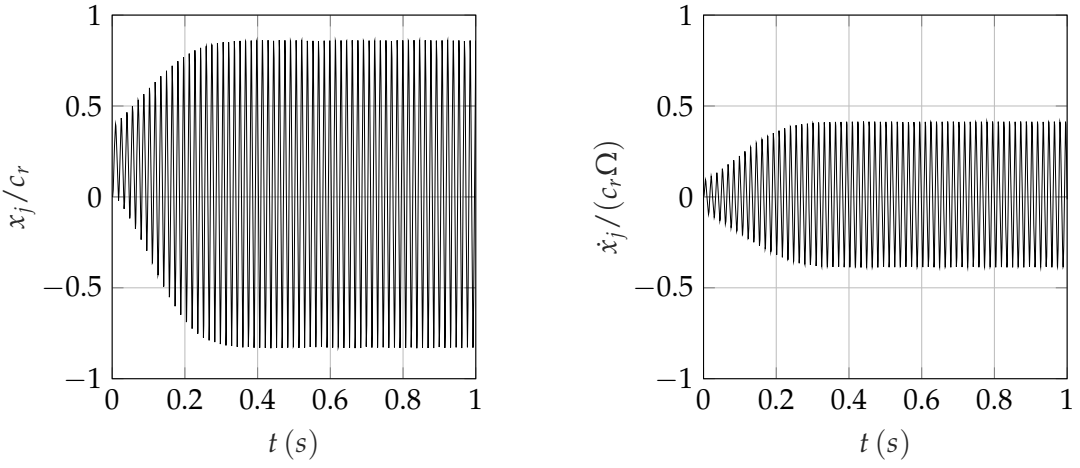

(a) x-displacement

(b) x-velocity

FIGURE 2.9: Displacement (a) and velocity (b) of the center of the disc in the x-direction at $\Omega = 850\,rad/s$. Bearing D100. Disc mass $m_d = 1\,kg$. Balanced rotor.

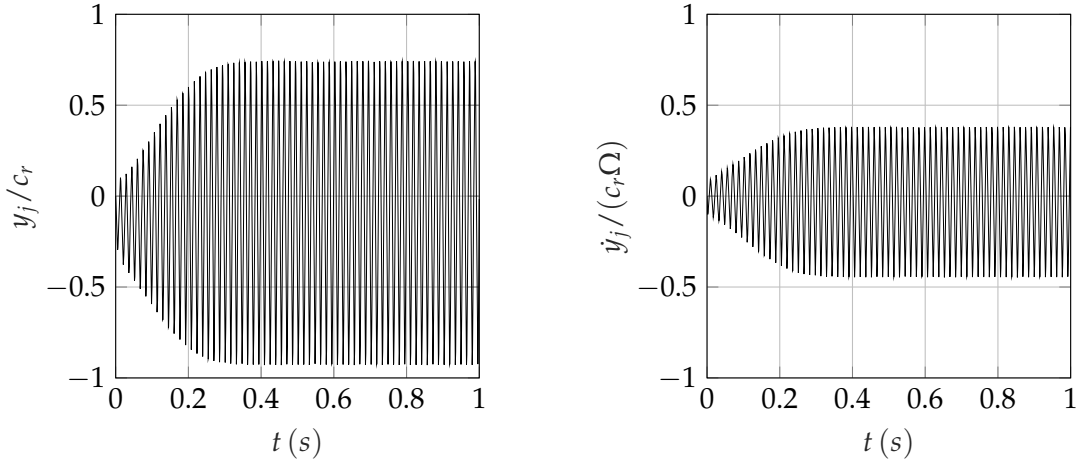

(a) y-displacement (b) y-velocity

FIGURE 2.10: Displacement (a) and velocity (b) of the center of the disc in the y-direction at $\Omega = 850\,rad/s$. Bearing D100. Disc mass $m_d = 1\,kg$. Balanced rotor

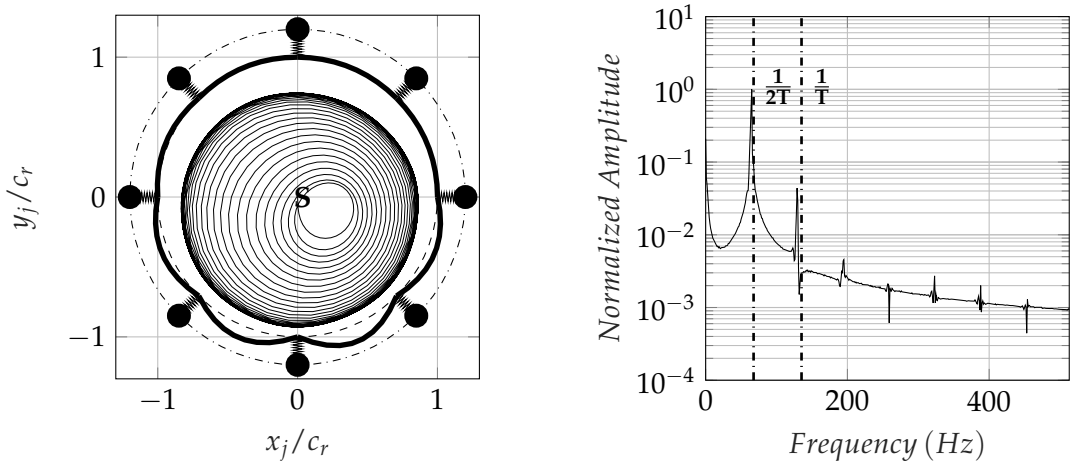

(a) orbit of the center of the disc (b) signal in the frequency domain

FIGURE 2.11: Orbit of the center of the disc at $\Omega = 850\,rad/s$ (a) and representation of the x-displacement of the center of the disc in the frequency domain (b). Bearing D100. Disc mass $m_d = 1\,kg$. Balanced rotor. The shape of the foil corresponds to the mid plane at $t = 1\,s$

The representation of the signal in the frequency domain concerns the x-displacement of the center of the disc. The signals concerning the y-displacement and the two velocities are omitted, as they are completely identical with that shown in Fig. 2.11. In Fig. 2.11 (b) T denotes the synchronous period, i.e $T = \frac{2\pi}{\Omega}$.
Until now, only the balanced system was examined. The addition of unbalance forces results in the response shown above in Fig. 2.12,2.13.

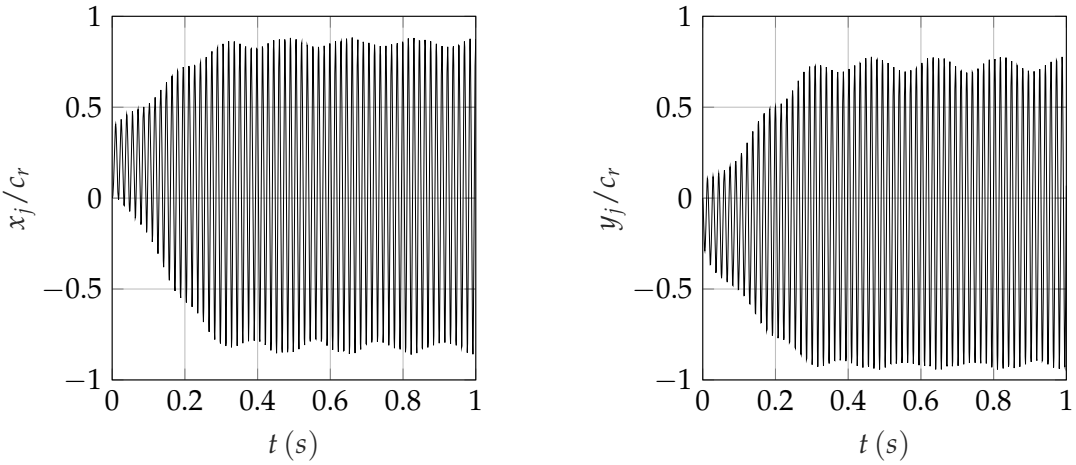

(a) x-displacement (b) y-displacement

FIGURE 2.12: x-displacement (a) and y-displacement (b) of the center of the disc at $\Omega = 850\,rad/s$. Bearing D100. Disc mass $m_d = 1\,kg$. Unbalance grade G6.3

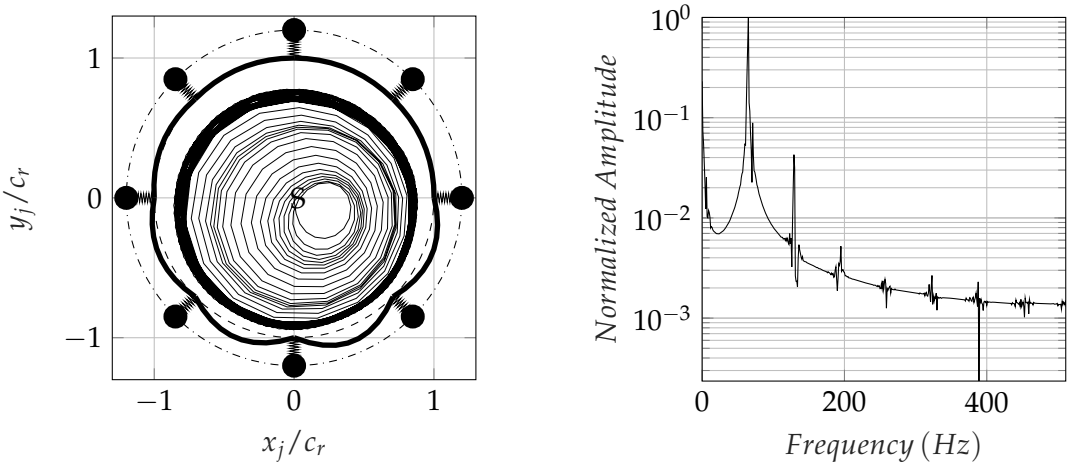

(a) orbit of the center of the disc (b) signal in the frequency domain

FIGURE 2.13: Orbit of the center of the disc at $\Omega = 850\,rad/s$ (a) and representation of the x-displacement of the center of the disc in the frequency domain (b). Bearing D100. Disc mass $m_d = 1\,kg$. Unbalance grade G6.3. The shape of the foil corresponds to the mid plane at $t = 1\,s$

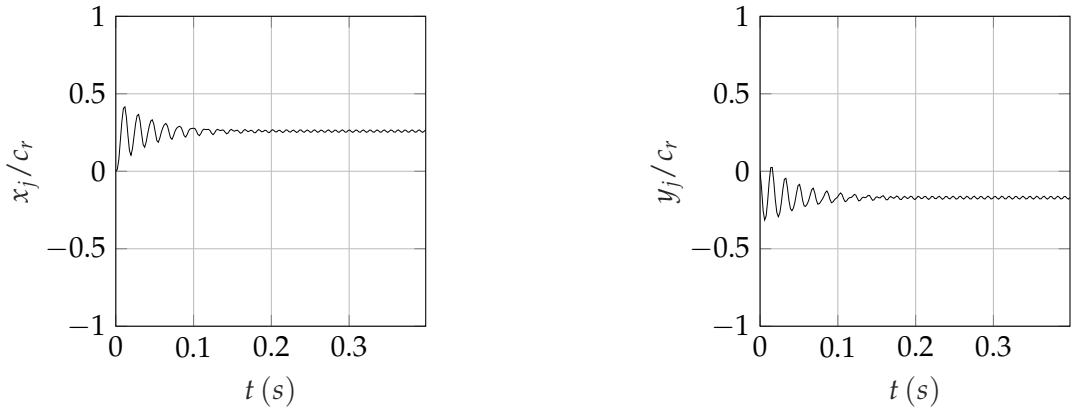

(a) x-displacement

(b) y-displacement

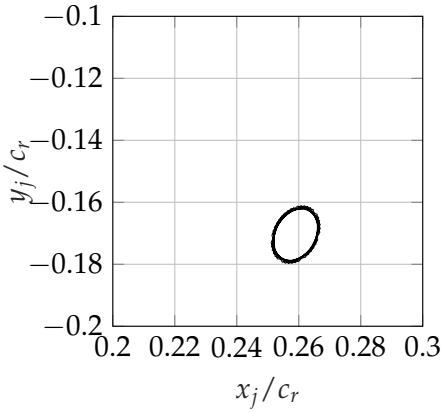

(c) steady state orbit

FIGURE 2.14: x-displacement (a), y-displacement (b) and orbit (c) of the center of the disc at $\Omega = 700\,rad/s$. Bearing D100. Disc mass $m_d = 1\,kg$. Unbalance grade G6.3.

As shown above, there is a great qualitative difference in the displacements of the center of the disc for the same unbalance grade and for a small change in rotational speed.

2.5.2 Results for the Bearing of Diameter D30

The results concerning the bearing D30 follow. The thickness of the top foil is $h_f = 0.1\,mm$, the Rayleigh loss factor is $\eta_h = 0.001\,s$, the stiffness of the springs is $k_f = 80\,\frac{N}{\mu m}$ and the displacement of the actuators is zero as well, i.e $\mathbf{q_a} = \mathbf{0}$.

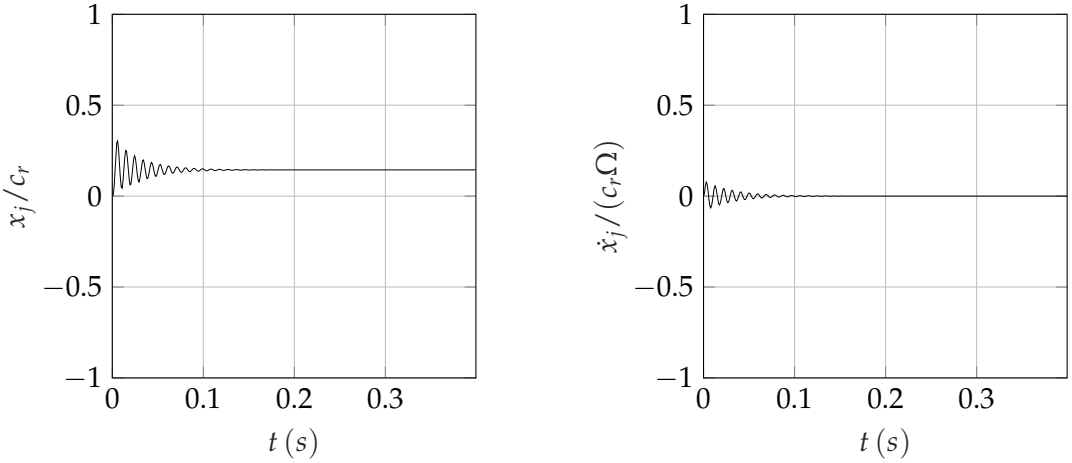

(a) x-displacement (b) x-velocity

FIGURE 2.15: Displacement (a) and velocity (b) of the center of the disc in the x-direction at $\Omega = 1300\,rad/s$. Bearing D30. Disc mass $m_d = 0.1\,kg$. Balanced rotor

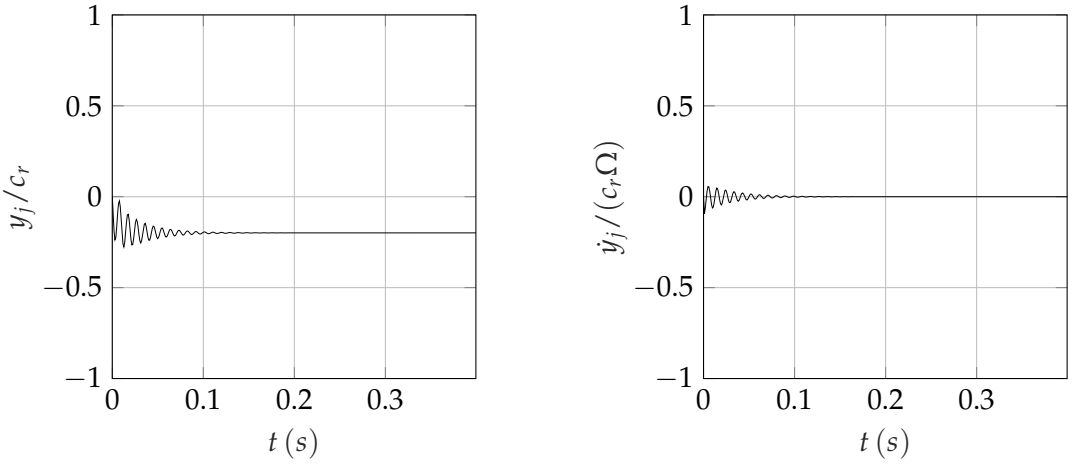

(a) y-displacement (b) y-velocity

FIGURE 2.16: Displacement (a) and velocity (b) of the center of the disc in the y-direction at $\Omega = 1300\,rad/s$. Bearing D30. Disc mass $m_d = 0.1\,kg$. Balanced rotor

It has been found that in the case of the bearing D30, the instability appears at higher rotational speeds relative to the bearing D100. Fig. 2.15 and 2.16 display the x and y- displacements and velocities of the center of the disc. The corresponding equilibrium point appears to be stable at $\Omega = 1300\,rad/s$, while the system with the bearing D100 has an unstable equilibrium point at $\Omega = 850 rad/s$. The stability of each system is thoroughly examined in Chapter 3.

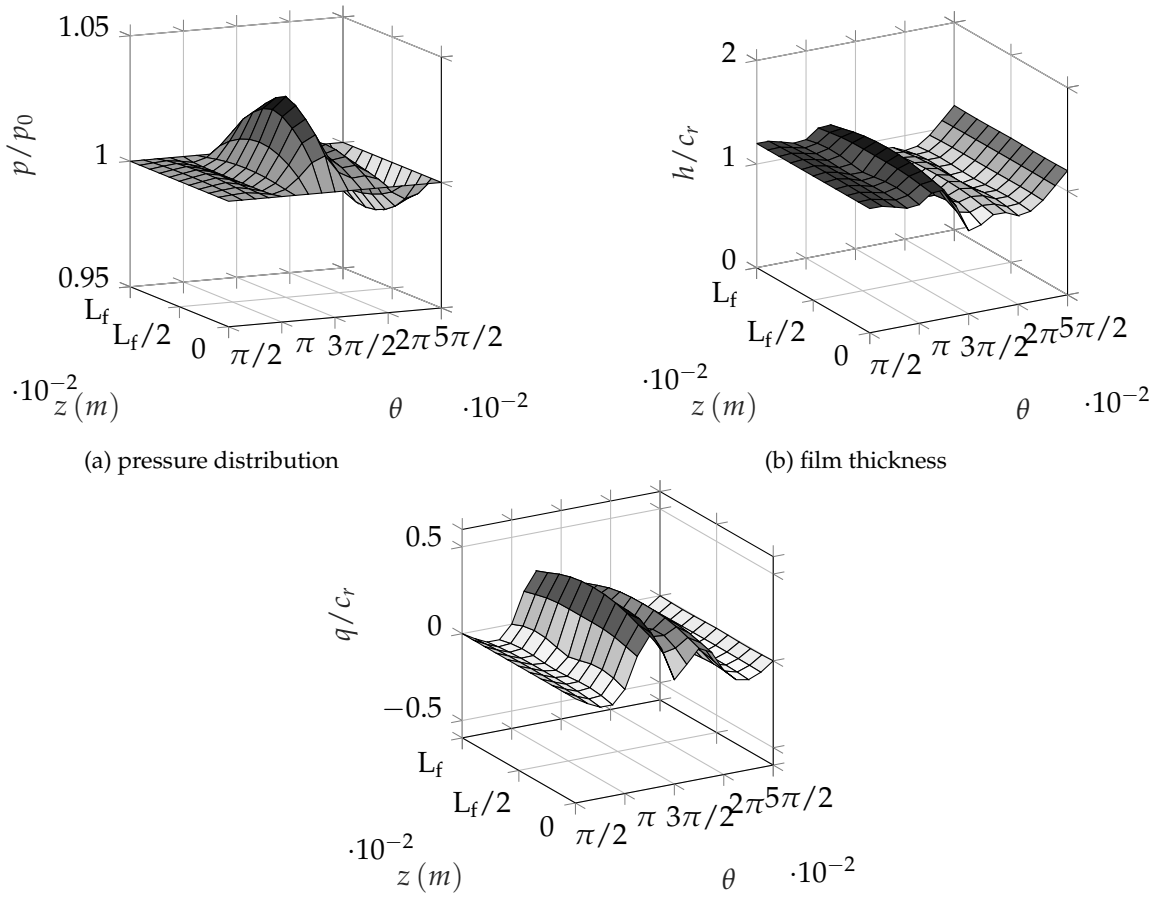

(a) pressure distribution

(b) film thickness

(c) foil deformation

FIGURE 2.17: Stable equilibrium pressure distribution (a), film thickness (b) and foil deformation (c) at $\Omega = 1300\,rad/s$. Bearing D30. Disc mass $m_d = 0.1\,kg$. Balanced rotor

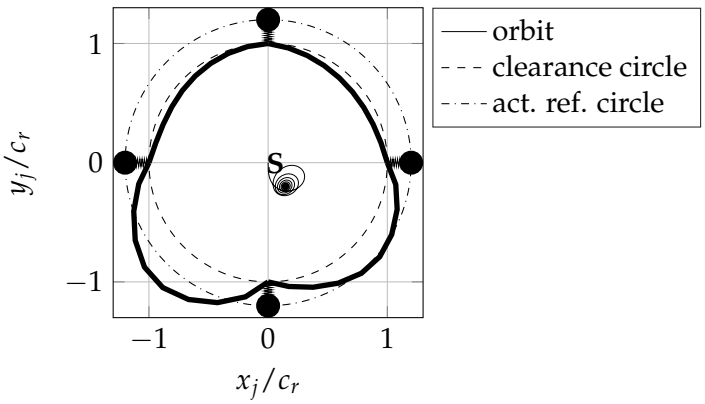

FIGURE 2.18: Orbit of the center of the disc at $\Omega = 1300\,rad/s$. Bearing D30. Balanced rotor. Disc mass $m_d = 0.1\,kg$. The shape of the foil corresponds to the mid plane at $t = 0.4\,s$.

Again, when the equilibrium point is unstable, a periodic solution emerges. That periodic solution is shown in Fig. 2.19 and 2.20. In Fig. 2.21 the orbit of the center of the disc is shown. The corresponding limit cycle is stable as it has been found that it attracts the orbit.

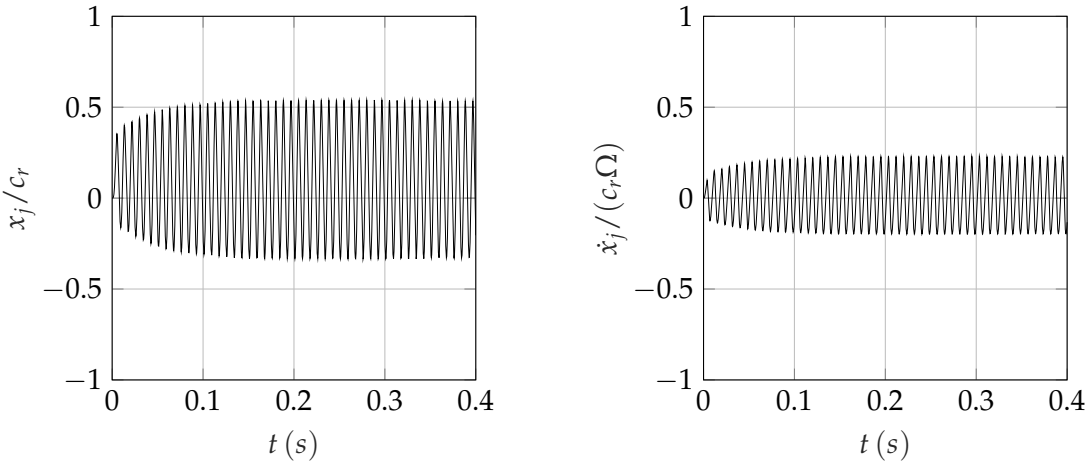

(a) x-displacement (b) x-velocity

FIGURE 2.19: Displacement (a) and velocity (b) of the center of the disc in the x-direction at $\Omega = 1550\,rad/s$. Bearing D30. Disc mass $m_d = 0.1\,kg$. Balanced rotor

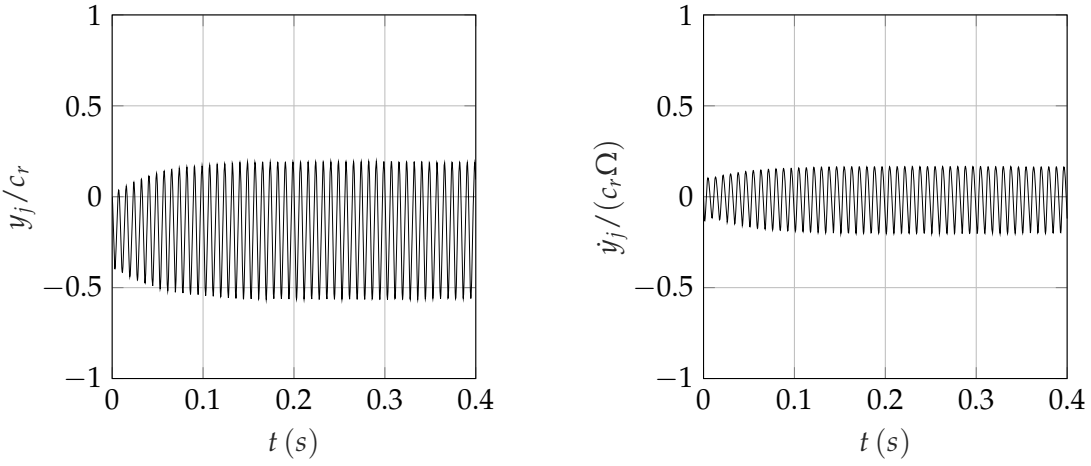

(a) y-displacement (b) y-velocity

FIGURE 2.20: Displacement (a) and velocity (b) of the center of the disc in the y-direction at $\Omega = 1550\,rad/s$. Bearing D30. Disc mass $m_d = 0.1\,kg$. Balanced rotor

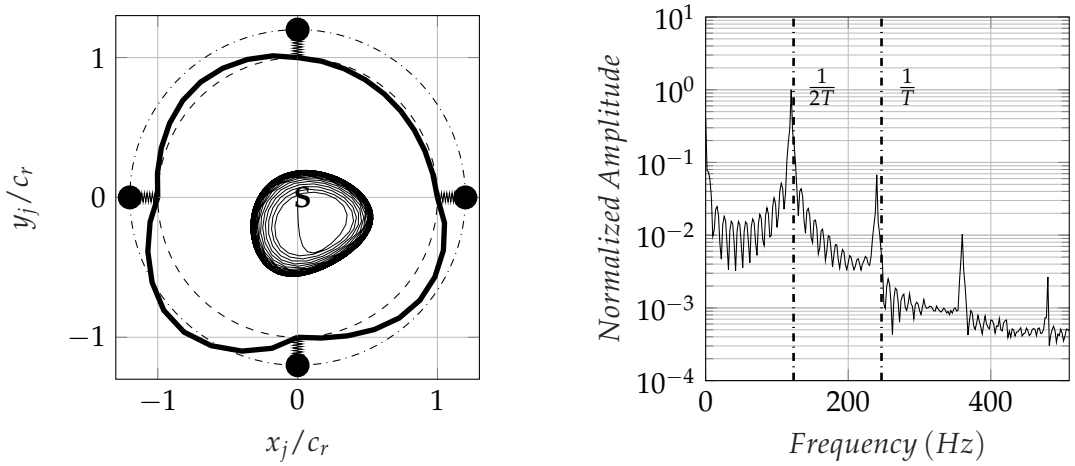

(a) orbit of the center of the disc

(b) signal in the frequency domain

FIGURE 2.21: Orbit of the center of the disc at $\Omega = 1550\,rad/s$ (a) and representation of the x-displacement of the center of the disc in the frequency domain (b). Bearing D30. Disc mass $m_d = 0.1\,kg$. Balanced rotor. The shape of the foil corresponds to the mid plane at $t = 0.4\,s$

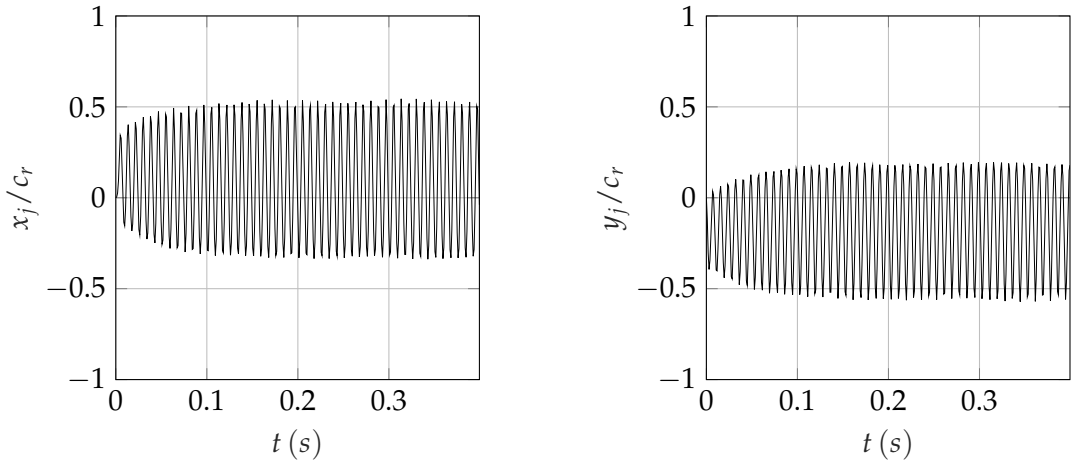

(a) x-displacement

(b) y-displacement

FIGURE 2.22: x-displacement (a) and y-displacement (b) of the center of the disc at $\Omega = 1550\,rad/s$. Bearing D30. Disc mass $m_d = 0.1\,kg$. Unbalance grade G2.5

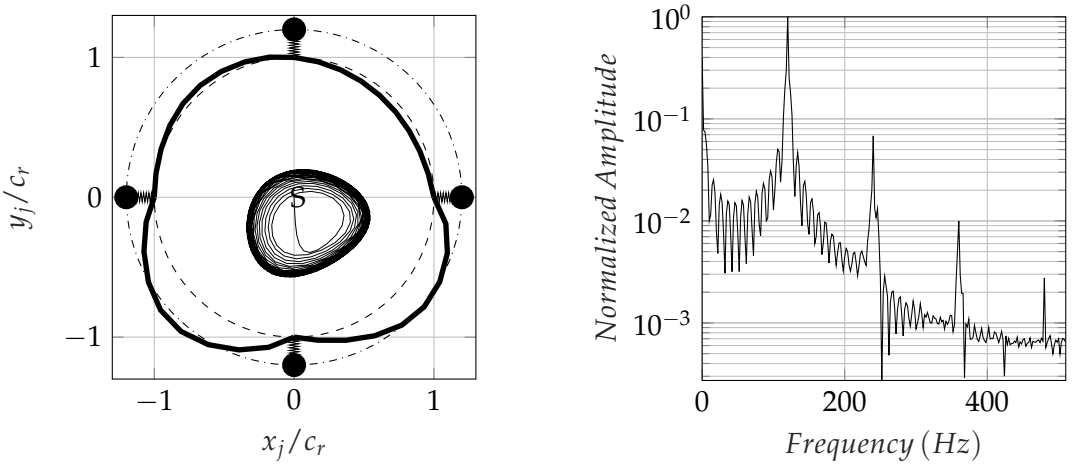

(a) orbit of the center of the disc

(b) signal in the frequency domain

FIGURE 2.23: Orbit of the center of the disc at $\Omega = 1550\,rad/s$ (a) and representation of the x-displacement of the center of the disc in the frequency domain (b). Bearing D30. Disc mass $m_d = 0.1\,kg$. Unbalance grade G2.5. The shape of the foil corresponds to the mid plane at $t = 0.4\,s$

Chapter 3

Application of Feedback Control

The main purpose of this Chapter is to exhibit a number of control techniques for the stabilization of unstable equilibrium points of the autonomous system. The stabilization of an equilibrium point results in the system reaching equilibrium asymptotically. In practice, the goal is for the system to reach sufficiently close to its equilibrium state in a finite time, which is called the setting time and is determined by the real part of the eigenvalues with the smallest real part. First, a linear control technique is investigated. The system is linearized around its equilibrium point and a feedback control law for the stabilization of this point is used, utilizing an observer [31]. Polynomial feedback control laws [32] are then considered, in order to stabilize the equilibrium point and eliminate possible Hopf Bifurcations [33]. Further to that, this technique appears to be applicable and in the case of existing unbalance forces, and results in steady state oscillations with significantly decreased amplitude and synchronous period. A design optimization follows, with goal to place the components of the equilibrium point concerning the displacements of the shaft to a desired location.

3.1 Stabilization via Linear Control

The autonomous balanced system is written in the form

$$\dot{\mathbf{x}} = \mathbf{f}\left(\mathbf{x}; \mathbf{q_a}, \Omega\right)$$

Suppose that the interest is to stabilize the system at a specific value of the rotational speed $\Omega = \Omega_i$, for fixed actuator displacements $\mathbf{q_a} = \mathbf{q_{a_0}}$. Then, the system is written as

$$\dot{\mathbf{x}} = \mathbf{f}\left(\mathbf{x}; \mathbf{q_{a_0}}, \Omega_i\right) = \mathbf{f}\left(\mathbf{x}\right)$$

The vector field $\mathbf{f}\left(\mathbf{x}\right)$ has an equilibrium point (fixed point) $\mathbf{x}^* \in \mathbb{R}^N$, which is the result of the solution of the equation

$$\mathbf{f}\left(\mathbf{x}\right) = 0$$

For this equilibrium point, the Jacobian matrix of the partial derivatives of the vector field $\mathbf{f}$ with respect to the state variables is calculated as

$$\mathbf{J} = \frac{\partial \mathbf{f}}{\partial \mathbf{x}}\Big|_{\substack{\mathbf{x}=\mathbf{x}^* \\ \mathbf{q_a}=\mathbf{q_{a_0}}}} = \begin{bmatrix} \frac{\partial f_1}{\partial x_1} & \frac{\partial f_1}{\partial x_2} & \cdots & \frac{\partial f_1}{\partial x_N} \\ \cdots & \cdots & \cdots & \cdots \\ \frac{\partial f_N}{\partial x_1} & \frac{\partial f_N}{\partial x_2} & \cdots & \frac{\partial f_N}{\partial x_N} \end{bmatrix} \in \mathbb{R}^{N \times N} \tag{3.1}$$

The stability of the equilibrium point is determined by the eigenvalues of the Jacobian matrix, according to the First Lyapunov Criterion [34]. If all the eigenvalues are

on the negative complex half-plane, i.e the real part of all eigenvalues is negative, then the equilibrium point is asymptotically stable. If at least one eigenvalue has positive real part, then the equilibrium point is unstable. If a number of eigenvalues are located on the imaginary axis, i.e the corresponding real parts are zero, and the other eigenvalues are on the negative complex half-plane, the stability of the equilibrium point cannot be decided using this criterion. Also, the matrix containing the partial derivatives of the vector field with respect to the actuators displacement is calculated as

$$\mathbf{B} = \frac{\partial \mathbf{f}}{\partial \mathbf{q_a}}\Big|_{\substack{\mathbf{x}=\mathbf{x}^* \\ \mathbf{q_a}=\mathbf{q_{a_0}}}} = \begin{bmatrix} \frac{\partial f_1}{\partial q_{a_1}} & \frac{\partial f_1}{\partial q_{a_2}} & \dots & \frac{\partial f_1}{\partial q_{a_M}} \\ \dots & \dots & \dots & \dots \\ \frac{\partial f_N}{\partial q_{a_1}} & \frac{\partial f_N}{\partial q_{a_2}} & \dots & \frac{\partial f_N}{\partial q_{a_M}} \end{bmatrix} \in \mathbb{R}^{N \times M} \tag{3.2}$$

The output of the system, namely the state variables that can be measured, will be the displacements and velocities of the journal. The output vector is, then

$$\mathbf{y} = \mathbf{C} \cdot \mathbf{x} \tag{3.3}$$

where $\mathbf{y} \in \mathbb{R}^4$ and $\mathbf{C} \in \mathbb{R}^{4 \times N}$

The linearized system around the equilibrium point is, then,

$$\begin{aligned} \delta \dot{\mathbf{x}} &= \mathbf{A} \cdot \delta \mathbf{x} + \mathbf{B} \cdot \delta \mathbf{q_a} \\ \delta \mathbf{y} &= \mathbf{C} \cdot \delta \mathbf{x} \end{aligned} \tag{3.4}$$

where $\mathbf{A} = \mathbf{J}$, $\delta \mathbf{x} = \mathbf{x} - \mathbf{x}^* \in \mathbb{R}^N$, $\delta \mathbf{q_a} = \mathbf{q_a} - \mathbf{q_{a_0}} \in \mathbb{R}^M$ and $\delta \mathbf{y} = \mathbf{y} - \mathbf{y}^* \in \mathbb{R}^4$. $\mathbf{y}^*$ is the output of the system, when $\mathbf{x} = \mathbf{x}^*$ for $\mathbf{q_a} = \mathbf{q_{a_0}}$.

The main goal to be achieved in this section, is the stabilization of unstable equilibrium points. By applying a state transformation to modal coordinates and rearranging the new state variables, the system becomes

$$\begin{aligned} \delta \dot{\mathbf{x}}_\mathbf{b} &= \mathbf{A_b} \cdot \delta \mathbf{x_b} + \mathbf{B_b} \cdot \delta \mathbf{q_a} \\ \delta \mathbf{y} &= \mathbf{C_b} \cdot \delta \mathbf{x_b} \end{aligned} \tag{3.5}$$

where $\mathbf{x_b} = \mathbf{T_b} \cdot \mathbf{x}$, $\mathbf{T_b}$ is the transformation matrix, $\mathbf{A_b} = \mathbf{T_b}^{-1} \cdot \mathbf{A} \cdot \mathbf{T_b}$, $\mathbf{B_b} = \mathbf{T_b}^{-1} \cdot \mathbf{B}$ and $\mathbf{C_b} = \mathbf{C} \cdot \mathbf{T_b}$. This transformation is shown in Appendix B. The matrix $\mathbf{T_b}$ is non singular and the matrices $\mathbf{A}$ and $\mathbf{A_b}$ have the same eigenvalues. Also, the new matrices are written in the form

$$\mathbf{A_b} = \begin{bmatrix} \mathbf{A_u} & \mathbf{O} \\ \mathbf{O} & \mathbf{A_s} \end{bmatrix}, \ \mathbf{B_b} = \begin{bmatrix} \mathbf{B_u} \\ \mathbf{B_s} \end{bmatrix}, \ \mathbf{C_b} = \begin{bmatrix} \mathbf{C_u} \, \mathbf{C_s} \end{bmatrix} \tag{3.6}$$

where $\mathbf{A_u}$ contains the eigenvalues with positive real part. The new state vector is written in the form

$$\delta \mathbf{x_b} = \left\{ \delta \mathbf{x_u} \ \delta \mathbf{x_s} \right\}^T \tag{3.7}$$

Note that the systems B.8 and 3.5 have the same input $\delta \mathbf{q_a}$ and output $\delta \mathbf{y}$. The two systems are uncoupled and the interest is centered on the unstable part

$$\delta \dot{\mathbf{x}}_\mathbf{u} = \mathbf{A_u} \cdot \delta \mathbf{x_u} + \mathbf{B_u} \cdot \delta \mathbf{q_a} \tag{3.8}$$

For the stabilization of this system, a feedback control law in the form

$$\delta \mathbf{q_a} = -\mathbf{K_g} \cdot \delta \hat{\mathbf{x}}_\mathbf{u} \tag{3.9}$$

is considered. In Eq. 3.9, $\delta \hat{\mathbf{x}}_\mathbf{u}$ is an estimation of the state variables $\delta \mathbf{x_u}$ provided by the observer and $\mathbf{K_g}$ is the gain matrix that places the eigenvalues of the corresponding closed loop system in the desired location and is calculated according to Ackermann's theory [35]. In any case, it has been found that the system $(\mathbf{A_u}, \mathbf{B_u})$ is fully controllable and the system $(\mathbf{A_u}, \mathbf{C_u})$ is fully observable. The closed loop equations then are

$$\begin{Bmatrix} \delta \dot{\mathbf{x}}_\mathbf{u} \\ \delta \dot{\tilde{\mathbf{x}}}_\mathbf{u} \end{Bmatrix} = \begin{bmatrix} \mathbf{A_u} - \mathbf{B_u} \cdot \mathbf{K_g} & \mathbf{B_u} \cdot \mathbf{K_g} \\ \mathbf{O} & \mathbf{A_u} - \mathbf{L} \cdot \mathbf{C_u} \end{bmatrix} \cdot \begin{Bmatrix} \delta \mathbf{x_u} \\ \delta \tilde{\mathbf{x}}_\mathbf{u} \end{Bmatrix} \tag{3.10}$$

In this equation, $\mathbf{L}$ is the observer gain matrix. The block diagram of the close loop system 3.1 is shown in Fig. 3.1. The Ackermann's theory for the construction of the gain matrices is shown in Appendix B. After the solution of the closed loop system equations, $\delta \mathbf{q_a}$ is calculated and the system of ODEs

$$\delta \dot{\mathbf{x}}_\mathbf{s} = \mathbf{A_s} \cdot \delta \mathbf{x_s} + \mathbf{B_s} \cdot \delta \mathbf{q_a} \tag{3.11}$$

is solved. Then, the response of the original state variables is calculated as $\mathbf{x} = \mathbf{T_b} \cdot \mathbf{x_b}$.

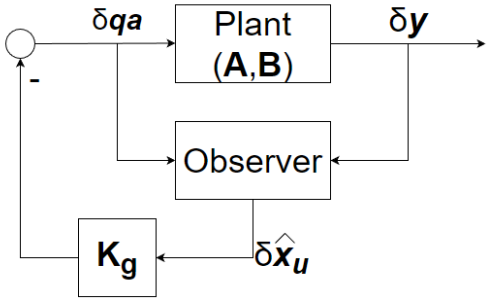

FIGURE 3.1: Close loop block diagram

First, the bearing D100 is investigated. In this case, the configuration of twenty four moving actuators shown in 2.3(a) is used. As shown in Fig. 2.9, for $\Omega = 850\,rad/s$, the system has an unstable equilibrium point. Therefore, in order to achieve stabilization, a close loop system for the placement of the eigenvalues is needed. The eigenvalues of the unstable subsystem 3.8 are placed in such location, that the closed loop system has setting time $t_s = 0.5\,s$ and the damped natural frequency remains the same. From literature, it is known that the setting time is approximately $t_s = -\frac{4}{Re(\lambda_{1,2})}$ [35]. These eigenvalues, which are the dominant eigenvalues of the close loop system, are $\lambda_{1,2} = -8 \pm j405$ and correspond to a damping ratio $\zeta \approx 0.02$. The eigenvalues of the observer are chosen to have the same imaginary part but ten times greater real part and they are $\lambda_{3,4} = -80 \pm j405$. Fig. 3.2 and 3.3 display the response of the open loop and the close loop system. The close loop system is stable and the displacements and velocities of the center of the disc reach equilibrium in approximately $t_s = 0.5\,s$. The error $\delta \tilde{\mathbf{x}}_\mathbf{u} = \delta \mathbf{x_u} - \delta \hat{\mathbf{x}}_\mathbf{u}$ tends to zero in 0.05 seconds as shown in Fig. 3.4(b). The orbit shown in Fig. 3.4(a) is initially attracted by the stable limit cycle. The activation of the control changes the qualitative behaviour of the response of the system and the orbit is attracted by the stable equilibrium or

fixed point. In this case, the close loop system has initial conditions that correspond to the final state of the open loop system and the initial time is the the time that the simulation of the open loop system ends. The initial conditions of the errors of the state variables are arbitrary chosen to be 0.3 times the initial conditions of those state variables.

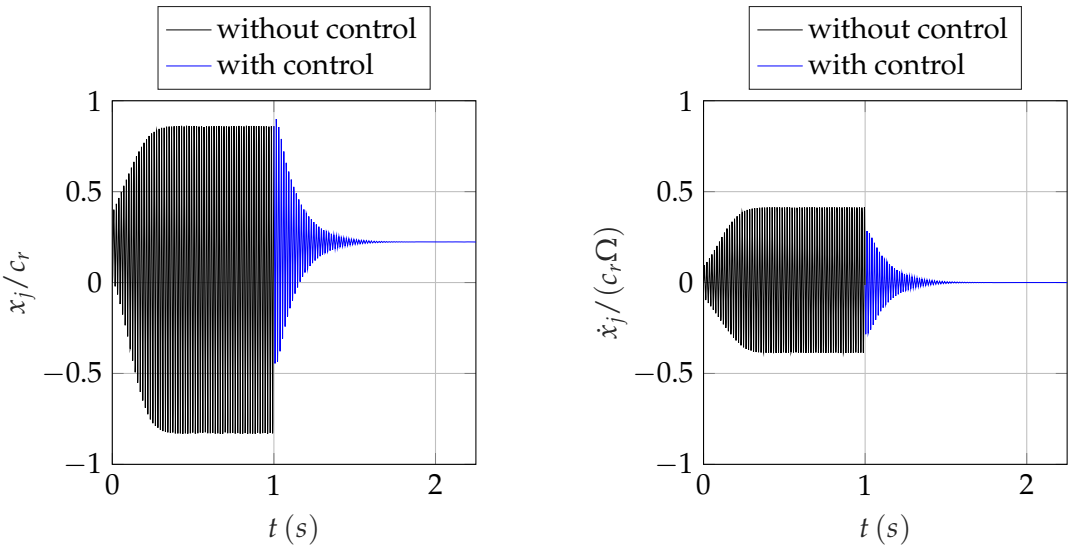

(a) x-displacement (b) x-velocity

FIGURE 3.2: Open and close loop x-displacement and velocity of the center of the disc at $\Omega = 850\,rad/s$.Bearing D100. Disc mass $m_d = 1\,kg$. Balanced rotor

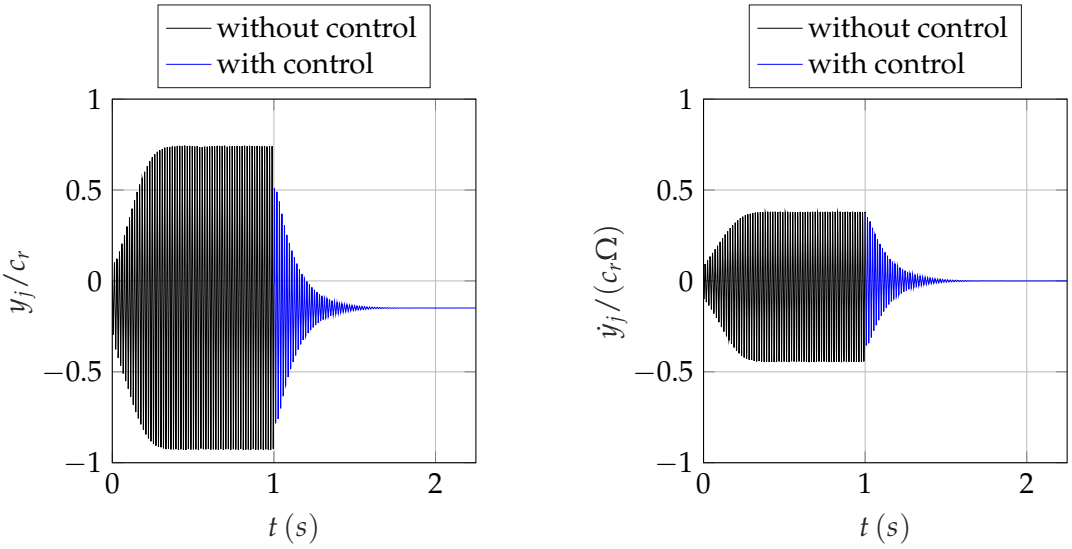

(a) y-displacement (b) y-velocity

FIGURE 3.3: Open and close loop x-displacement and velocity of the center of the disc at $\Omega = 850\,rad/s$.Bearing D100. Disc mass $m_d = 1\,kg$. Balanced rotor

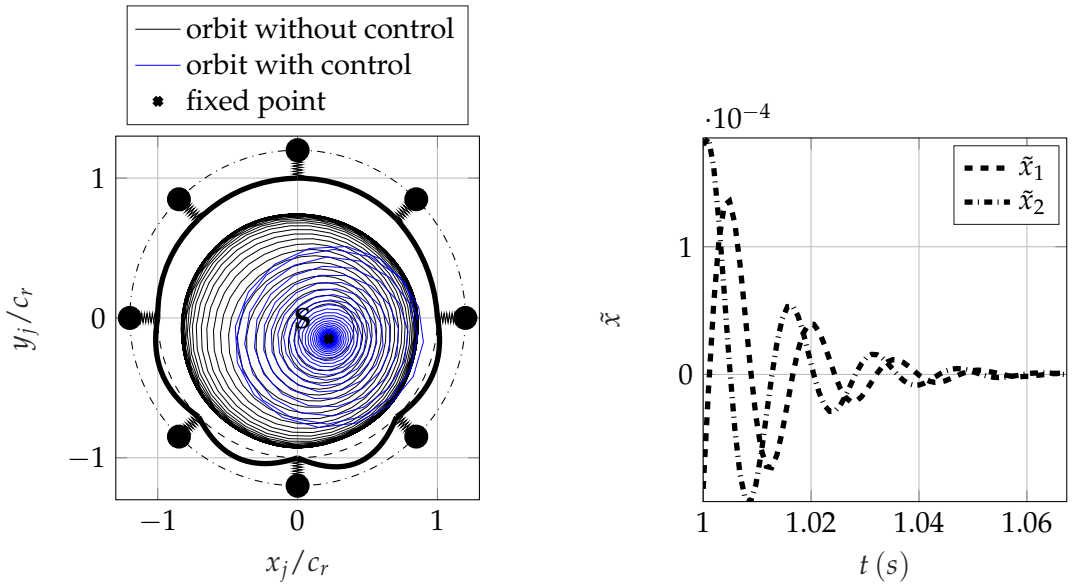

(a) Open and close loop orbit of the center of the disc

(b) Error of the closed loop system state variables

FIGURE 3.4: (a) Orbit of the center of the disc at $\Omega = 850 rad/s$. Disc mass $m_d = 1\,kg$. Balanced rotor. The shape of the top foil corresponds to the equilibrium point and (b) error resulting from the estimations of the values of the state variables

The pressure distribution, the film thickness and the foil deformation at the equilibrium state of the system are shown in Fig. 3.5. It should be noted that the control law used in order to stabilize the system does not change the equilibrium point but only the stability of it.

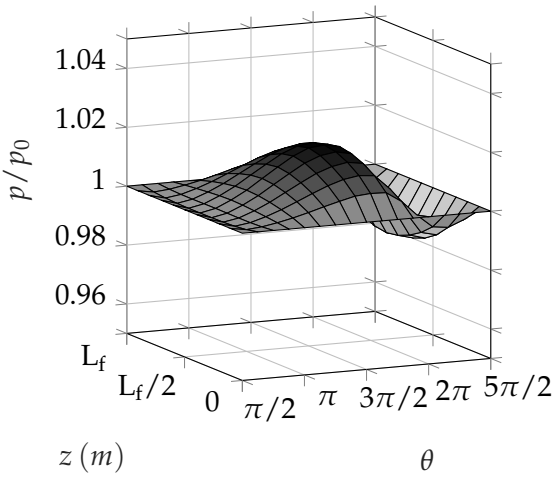

(a) pressure distribution

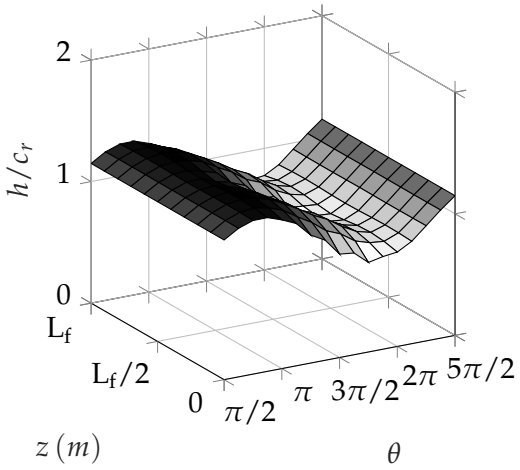

(b) film thickness

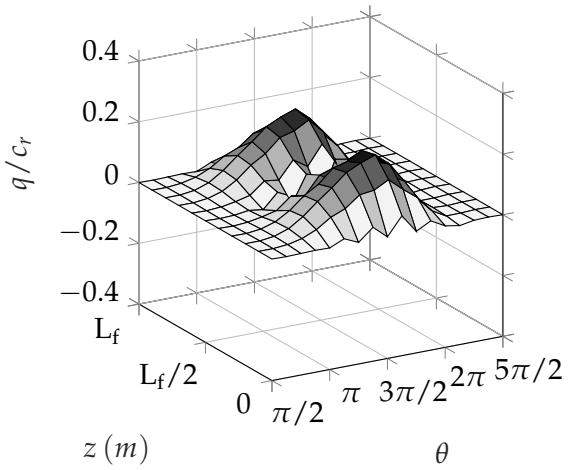

(c) foil deformation

FIGURE 3.5: Stable equilibrium pressure distribution (a), film thickness (b) and foil deformation (c) at $\Omega = 850\,rad/s$. Bearing D100. Disc mass $m_d = 1\,kg$. Balanced rotor

Concerning the bearing D30, dealing with instability is done in the same way. Twelve moving actuators are used, as shown in Fig. 2.3(b). The setting time has been found that can reach the value of $t_s = 0.1\,s$ and the observer is chosen to be ten times faster. The damped natural frequency of the eigenvalues of the close loop system is again the same as the one of the eigenvalues of the open loop system. Therefore, the eigenvalues of the close loop system are $-40 \pm j738$ and $-400 \pm j738$. Fig. 3.6 and 3.7 display the displacements and velocities of the open and close loop systems. After the initiation of the control, the system reaches equilibrium after time $t = 0.1\,s$, which is the desired setting time. The orbit of the close loop system, shown in Fig. 3.8, is attracted by the stable fixed point. In Fig. 3.9, the pressure distribution, the film thickness and the foil deformation of the equilibrium state are shown.

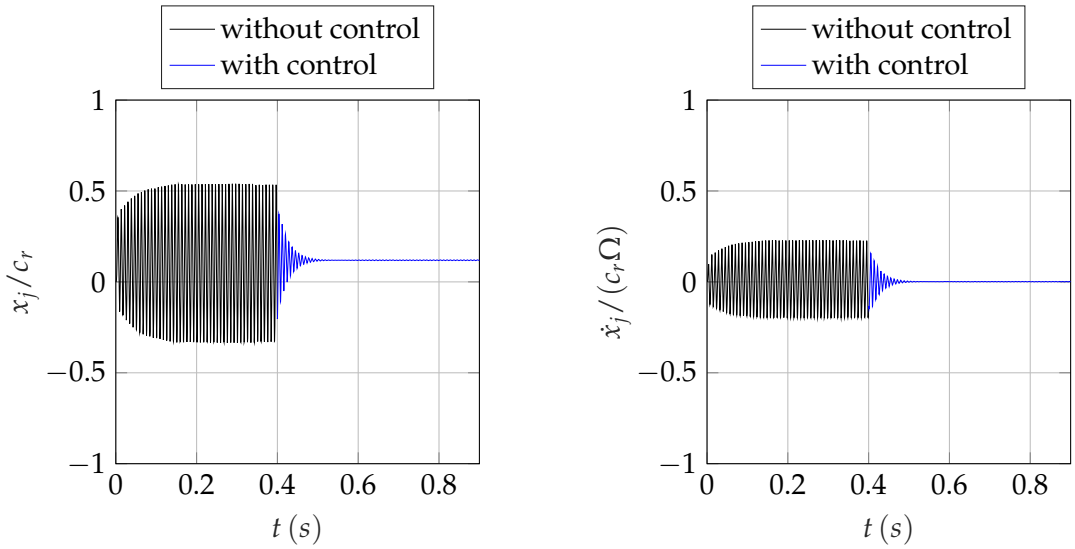

(a) x-displacement (b) x-velocity

FIGURE 3.6: Open and close loop x-displacement and velocity of the center of the disc at $\Omega = 1550\,rad/s$.Bearing D30. Disc mass $m_d = 0.1\,kg$. Balanced rotor

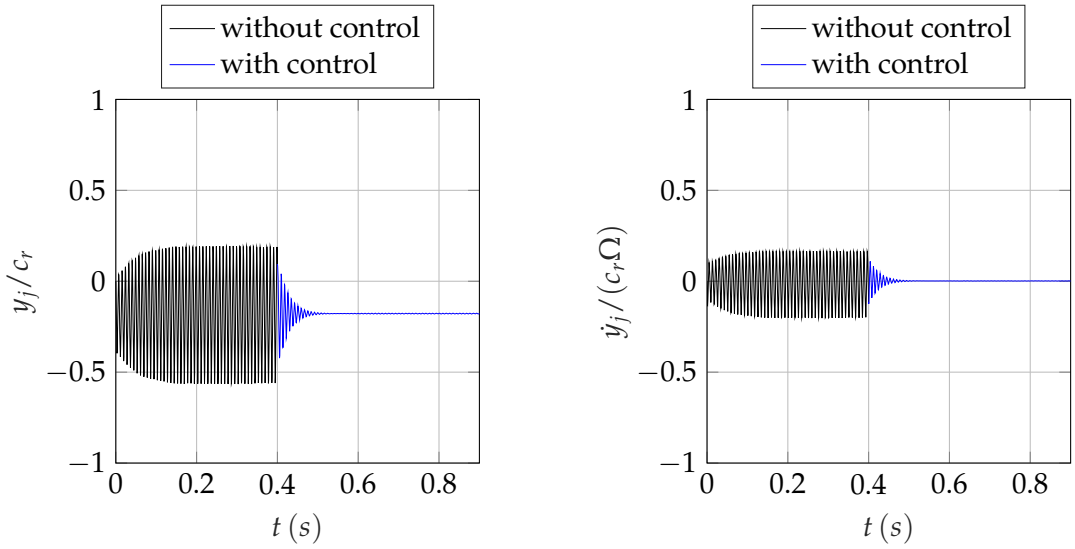

(a) y-displacement (b) y-velocity

FIGURE 3.7: Open and close loop y-displacement and velocity of the center of the disc at $\Omega = 1550\,rad/s$.Bearing D30. Disc mass $m_d = 0.1\,kg$. Balanced rotor

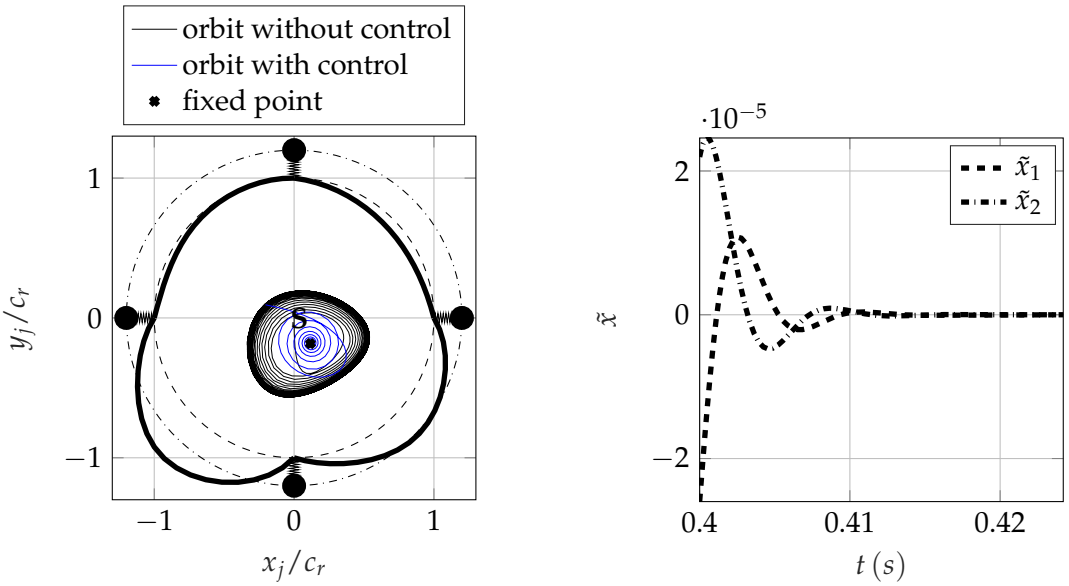

(a) Open and close loop orbit of the center of the disc

(b) Error of the closed loop system state variables

FIGURE 3.8: (a) Orbit of the center of the disc at $\Omega = 1550 rad/s$. Disc mass $m_d = 0.1\,kg$. Balanced rotor. The shape of the top foil corresponds to the equilibrium point and (b) error resulting from the estimations of the values of the state variables

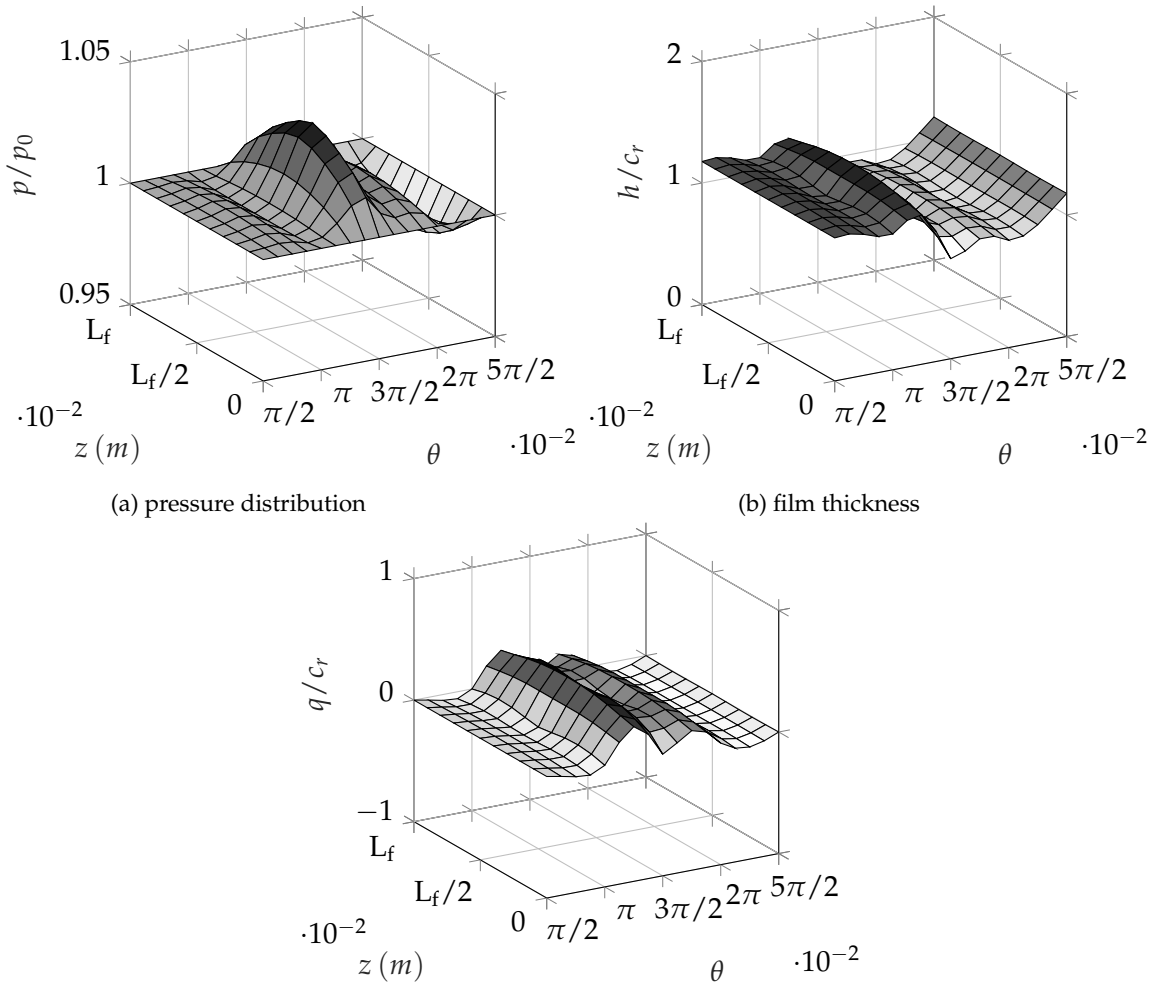

(a) pressure distribution

(b) film thickness

(c) foil deformation

FIGURE 3.9: Stable equilibrium pressure distribution (a), film thickness (b) and foil deformation (c) at $\Omega = 1550\,rad/s$. Bearing D30. Disc mass $m_d = 0.1\,kg$. Balanced rotor

3.2 Hopf Bifurcation Control via Polynomial Feedback

Again, the autonomous balanced system 3.1 is considered. From Eq. 2.14 it follows that the system can be written in the form

$$\dot{\mathbf{x}} = \mathbf{f}\left(\mathbf{x}; \mathbf{q_a}, \Omega\right) = \mathbf{g}\left(\mathbf{x}; \Omega\right) + \mathbf{G} \cdot \mathbf{q_a} \tag{3.12}$$

where $\mathbf{G}$ is a $N \times M$ constant matrix. Suppose that the reference displacement of the actuators is $\mathbf{q_{a_0}}$, then for every discrete value of the rotational speed Ω_i a equilibrium point occurs. Therefore, there is a sequence of equilibrium points

$$\left(\mathbf{x}_1^*, \Omega_1\right), ..., \left(\mathbf{x}_m^*, \Omega_m\right), \ \left(\mathbf{x}_i^*, \Omega_i\right) \in \mathbb{R}^{N+1} \tag{3.13}$$

each corresponding to a discrete value of the rotational speed. Their stability is examined using the First Lyapunov Criterion. In this system, it has been observed that the system is stable until a threshold value of the rotational speed,Ω_{th}, and then becomes unstable. This type of bifurcation is called Hopf Bifurcation [33, 32] and for it to happen, the following conditions must apply:

- $\mathbf{f}(\mathbf{x_{th}}; \Omega_{th}) = 0$, i.e the point $(\mathbf{x_{cr}}, \Omega_{th})$ is a equilibrium point
- the dominant eigenvalues of the Jacobian matrix $\lambda_{1,2} = \hat{a}(\Omega_{th}) \pm j\hat{b}(\Omega_{th})$ are located on the imaginary axis, i.e $\hat{a}(\Omega_{th}) = 0$, and
- $\left.\frac{d\hat{a}}{d\Omega}\right|_{\Omega=\Omega_{th}} \neq 0$

The goal is to design a feedback control law, that will eliminate this Hopf Bifurcation. First the stabilization of a fixed point is considered and then the elimination of Hopf Bifurcations is presented.

3.2.1 Stabilization of Unstable Fixed Points

Suppose the case where the Hopf Bifurcation has already occurred and the equilibrium point corresponding to the rotational speed Ω_k is unstable. The goal is to stabilize the system, without changing the equilibrium point. The output in this case is again the displacements and velocities of the journal, so the feedback control has to be designed using only these state variables, therefore $\mathbf{q_a} = \mathbf{q_a}\left(x_j, \dot{x}_j, y_j, \dot{y}_j\right)$.

For $\Omega = \Omega_k$ and $\mathbf{q_a} = \mathbf{q_{a_0}}$, the system

$$\dot{\mathbf{x}} = \mathbf{f}(\mathbf{x}; \mathbf{q_{a_0}}, \Omega_k) = \mathbf{f}(\mathbf{x}; \mathbf{q_{a_0}}) = \mathbf{g}(\mathbf{x}) + \mathbf{G} \cdot \mathbf{q_{a_0}} \tag{3.14}$$

has a equilibrium point $\mathbf{x}_k^*$, therefore

$$\mathbf{g}(\mathbf{x}_k^*) + \mathbf{G} \cdot \mathbf{q_{a_0}} = 0 \tag{3.15}$$

Therefore, in order to maintain the same equilibrium point, the condition $\mathbf{q_a}\left(x_j^*, \dot{x}_j^*, y_j^*, \dot{y}_j^*\right) = \mathbf{q_{a_0}}$ must be satisfied, where $x_j^*, \dot{x}_j^*, y_j^*, \dot{y}_j^*$ are the equilibrium components corresponding to the journal. A linear polynomial feedback law, proposed by Chen [32], is

$$\mathbf{q_a} = -\mathbf{k_1}\left(x_j - x_j^*\right) - \mathbf{k_2}\left(\dot{x}_j - \dot{x}_j^*\right) - \mathbf{k_3}\left(y_j - y_j^*\right) - \mathbf{k_4}\left(\dot{y}_j - \dot{y}_j^*\right) + \mathbf{q_{a_0}} \tag{3.16}$$

where $\mathbf{k_i} \in \mathbb{R}^M$. It is clear, that when evaluated at the eq. point only the quantity $\mathbf{q_{a_0}}$ remains, so the condition 3.15 is satisfied. The closed loop system is

$$\dot{\mathbf{x}} = \mathbf{g}(\mathbf{x}) + \mathbf{G} \cdot \mathbf{q_a}\left(x_j, \dot{x}_j, y_j, \dot{y}_j\right) = \mathbf{f_{cl}}(\mathbf{x}) \tag{3.17}$$

The gain vectors $\mathbf{k_i}$ are such, that the Jacobian matrix corresponding to the closed-loop system has only eigenvalues with negative real parts. Also, they can be chosen in such way, that the dominant eigenvalues have real parts corresponding to a desired setting time $t_s \approx -\frac{4}{Re(\lambda_{1,2})}$, where $\lambda_{1,2}$ are the dominant eigenvalues. For simplicity, the gains are chosen in such way that $\mathbf{k_i} = k_i \begin{Bmatrix} 1 & 1 & ... & 1 \end{Bmatrix}^T$. The gains are calculated using an optimization procedure, calculating the Jacobian matrix at each step. The objective function is

$$min_{obj} = |Re(\lambda_{1,2}) + \frac{4}{ts}| \tag{3.18}$$

choosing the desired t_s. For the implementation of the above, the *patternsearch* function of the *Matlab Global Optimization Toolbox* was used.

In this case, only the bearing D100 is investigated. The actuators in the second row are moving, while the ones on the first and the third row are static, as shown in Fig. 2.4(a). The setting time is chosen to be $t = 0.5\,s$. Again, the close loop system has initial conditions that correspond to the final state of the simulation of the open loop system.

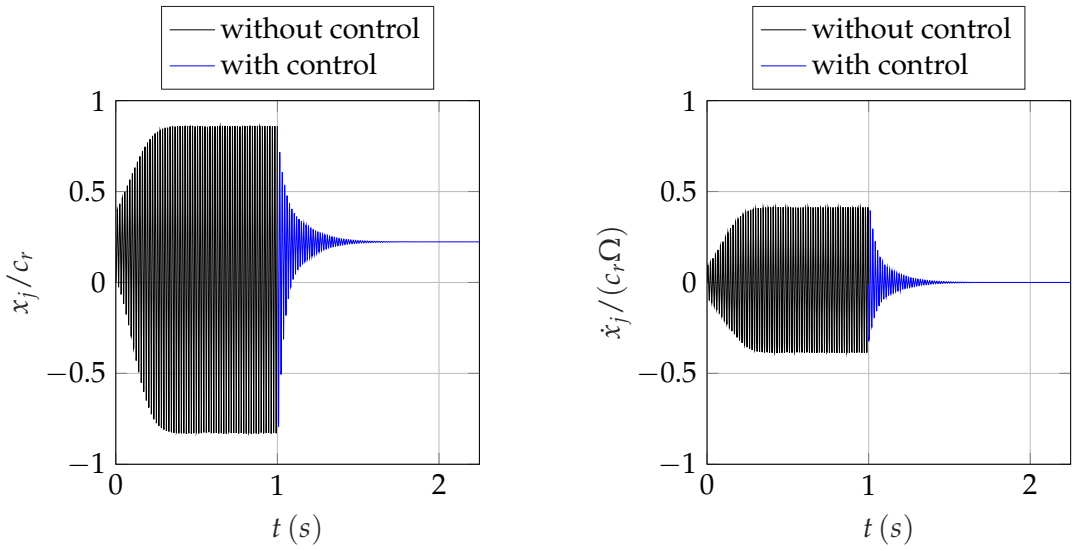

(a) x-displacement (b) x-velocity

FIGURE 3.10: Open and close loop x-displacement and velocity of the center of the disc at $\Omega = 850\,rad/s$.Bearing D100. Disc mass $m_d = 1\,kg$. Balanced rotor

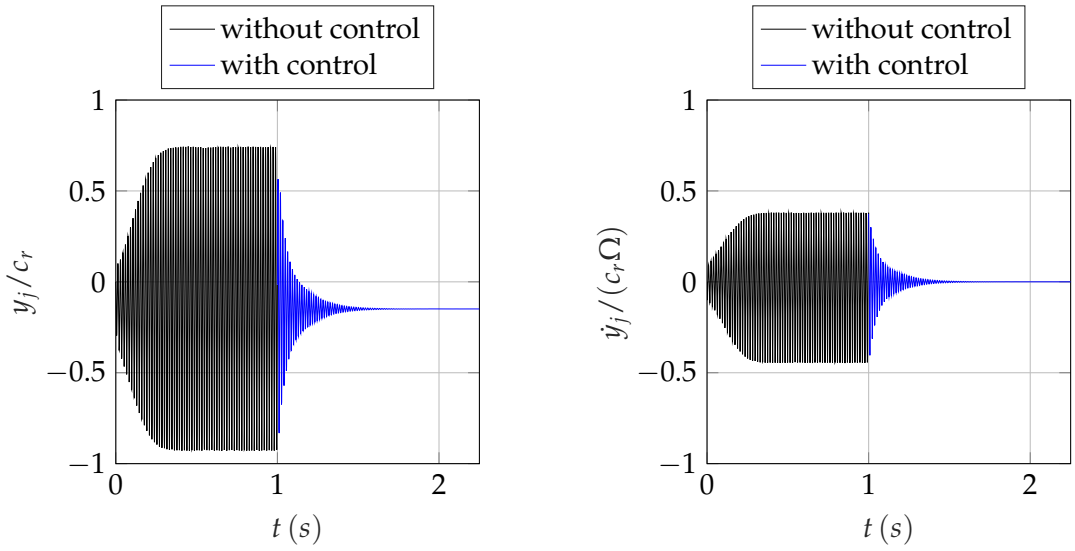

(a) y-displacement (b) y-velocity

FIGURE 3.11: Open and close loop y-displacement and velocity of the center of the disc at $\Omega = 850\,rad/s$. Bearing D100. Disc mass $m_d = 1\,kg$. Balanced rotor

Fig. 3.10 and 3.11 show the response of the journal. The orbit of the journal is shown in Fig. 3.13. The close loop system reaches equilibrium in time $t = 0.5\,s$. The displacement of the actuators and the required voltage input are shown in Fig. 3.12(a)

and 3.12(b) respectively.

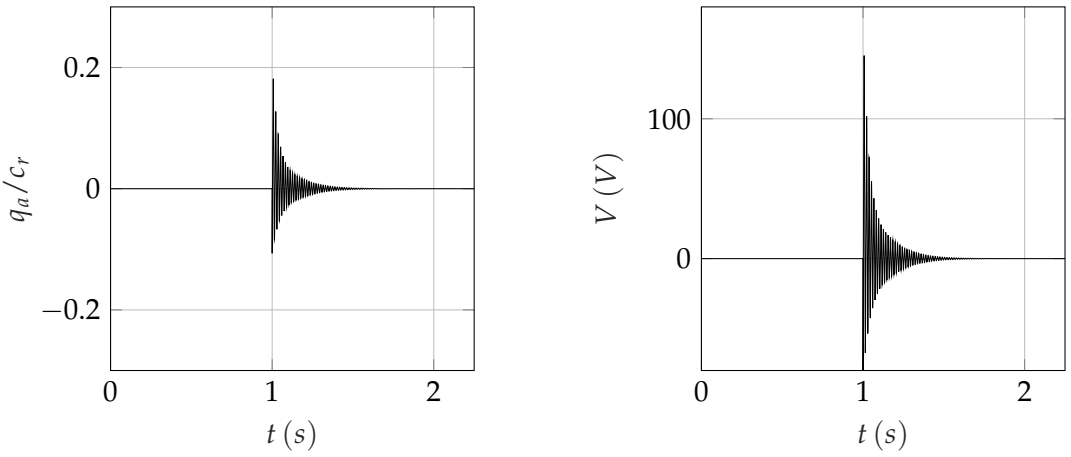

(a) displacement of the actuators

(b) voltage input

FIGURE 3.12: Actuators displacement (a) and voltage input (b) of the open and close loop system at $\Omega = 850\,rad/s$. Bearing D100. Disc mass $m_d = 1\,kg$. Balanced rotor

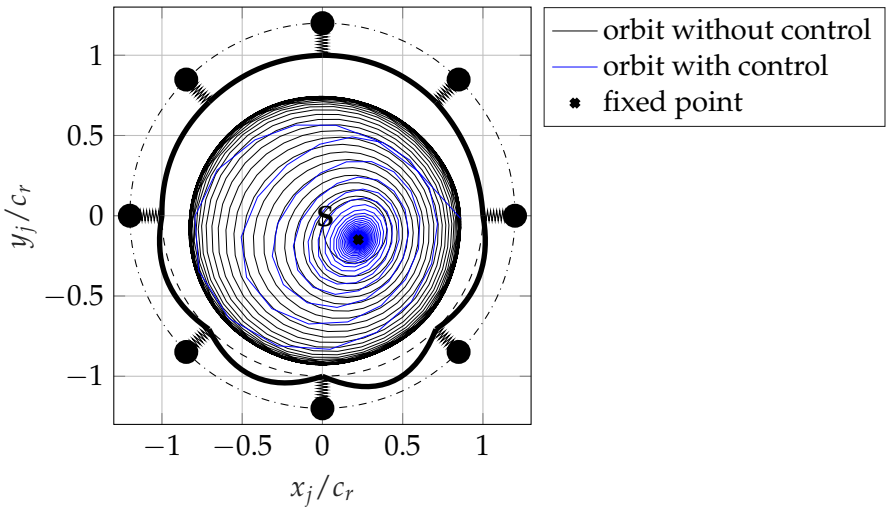

FIGURE 3.13: Open and close loop orbit of the center of the disc at $\Omega = 850\,rad/s$. Bearing D100. Disc mass $m_d = 1\,kg$. Balanced rotor

This control law, similar to the linear control technique that was used, does not change the equilibrium point of the system. Therefore, the stable equilibrium pressure distribution, film thickness and foil deformation are the same as the ones exhibited in the section of the Linear control and are shown in Fig. 3.5.

Then, it is desirable to examine the behavior of the closed-loop system to external perturbations. For this, an external lateral force with magnitude equal to $2.5m_d$ is applied to the disc. This force is parallel to the y-axis of the cross section of the journal and is applied before the system reaches equilibrium. As a result, the disc oscillates with reduced amplitude, until it finally reaches equilibrium, as shown in Fig. 3.14 and 3.15. The corresponding displacement of the actuators and voltage input are shown in 3.16.

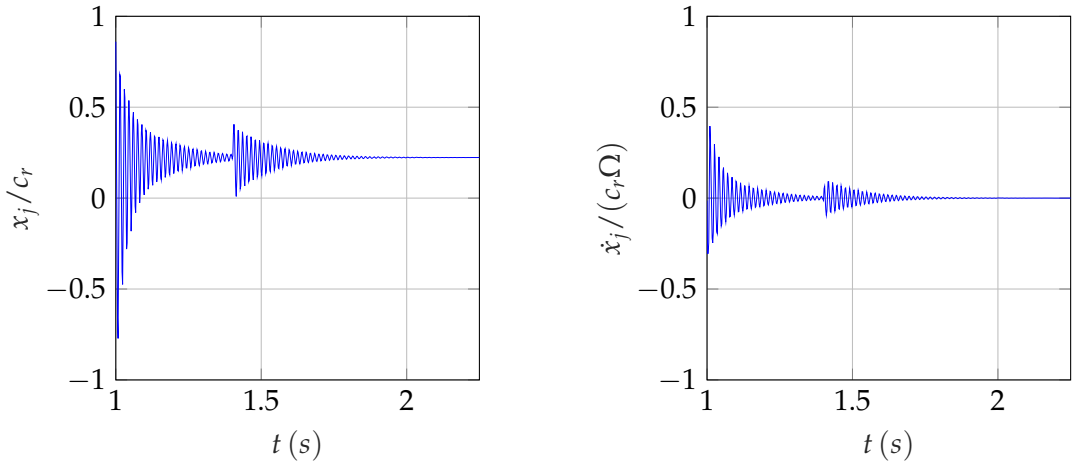

(a) x-displacement (b) x-velocity

FIGURE 3.14: Displacement (a) and velocity (b) in the x-direction of the center of the disc of the perturbed system at $\Omega = 850\,rad/s$. Bearing D100. Disc mass $m_d = 1\,kg$. Balanced rotor

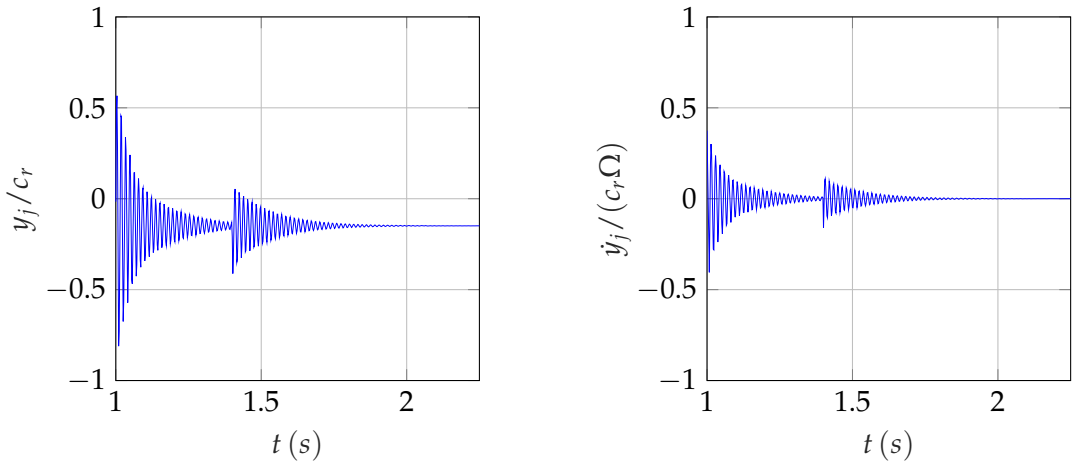

(a) y-displacement (b) y-velocity

FIGURE 3.15: Displacement (a) and velocity (b) in the y-direction of the center of the disc of the perturbed system at $\Omega = 850\,rad/s$. Bearing D100. Disc mass $m_d = 1\,kg$. Balanced rotor

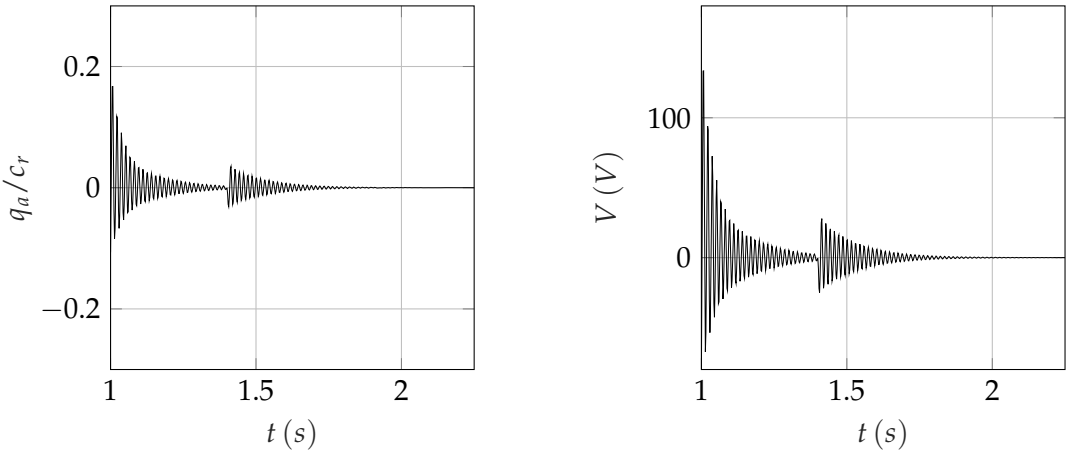

(a) displacement of the actuators

(b) voltage input

FIGURE 3.16: Actuators displacement (a) and voltage input (b) of the perturbed close loop system at $\Omega = 850\,rad/s$. Bearing D100. Disc mass $m_d = 1\,kg$. Balanced rotor

In the case of the unbalanced system, it has been found that the same control law of the corresponding autonomous system results in a steady state response with significantly reduced amplitude and synchronous period. This happens because, despite the fact that the principle of superposition is not applicable in nonlinear systems, it has been experimentally found that for small unbalance grades the superposition of the balanced system with the unbalance forces approaches sufficiently the real system. In Fig. 3.17 the displacements of the center of the disc are shown. Fig. 3.18 displays the steady state orbit and x-displacement of the center of the disc. The rotor oscillates around the equilibrium point of the autonomous system with period $T = 2\pi/\Omega$ and with a small amplitude in comparison with the open loop system.

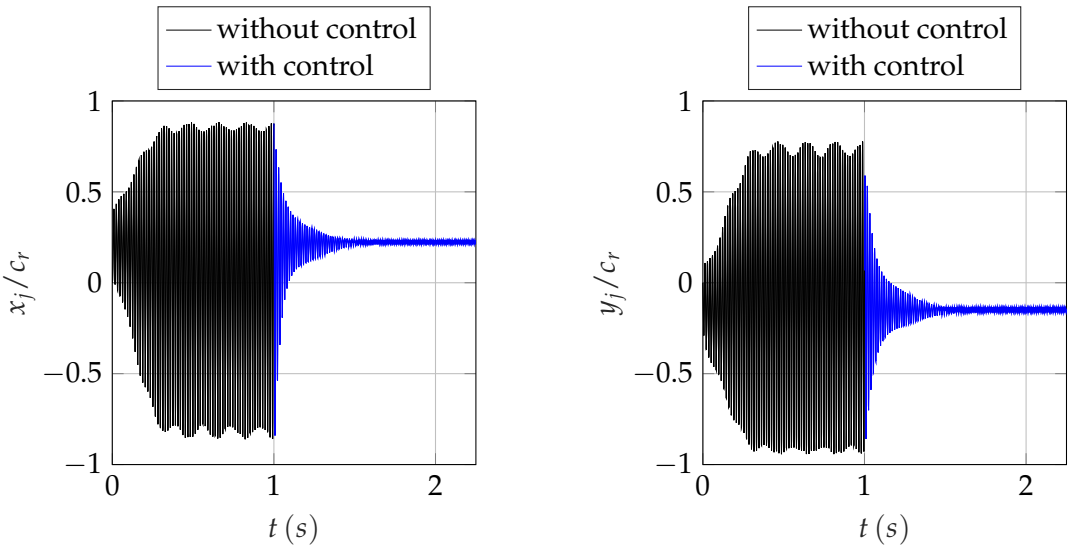

(a) x-displacement

(b) y-displacement

FIGURE 3.17: x (a) and y (b) displacement of the center of the disc of the open and close loop system at $\Omega = 850\,rad/s$. Bearing D100. Disc mass $m_d = 1\,kg$. Unbalance grade G6.3

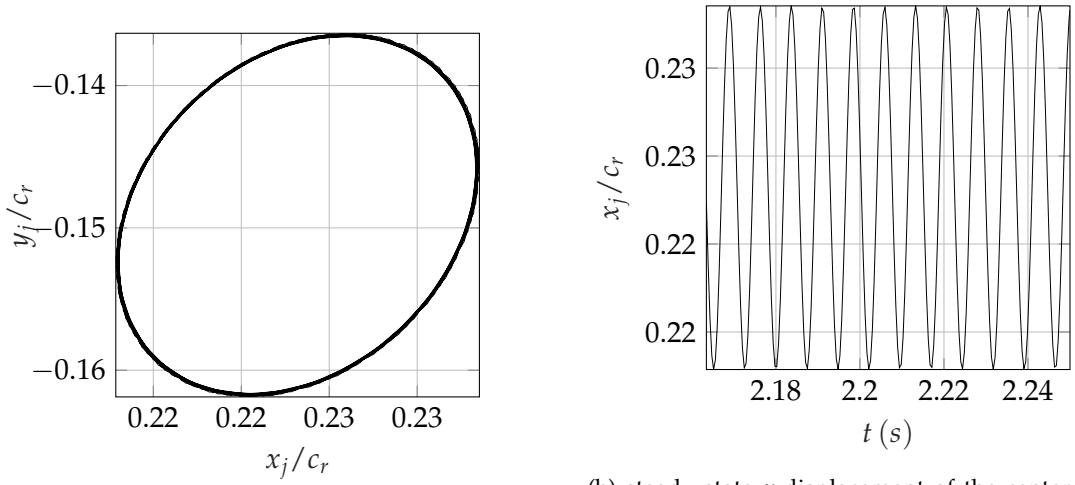

(a) steady state orbit

(b) steady state x-displacement of the center of the disc

FIGURE 3.18: Steady state response of the center of the disc at $\Omega = 850\,rad/s$. Bearing D100. Disc mass $m_d = 1\,kg$. Unbalance grade G6.3

3.2.2 Hopf Bifurcation Elimination

In order to eliminate the Hopf bifurcation from the entire range of rotational speed of the system, a polynomial feedback control law is designed for every discrete value of the rotational speed, see Eq. 3.16. The gains $\mathbf{k_i}$ are functions of the rotational speed Ω, therefore $\mathbf{k_i} = \mathbf{k_i}(\Omega)$ and are calculated by performing an optimization procedure for every Ω_i, where the corresponding equilibrium point is unstable, with desired setting time $t_s = 0.5\,s$.

The results concerning the bearing D30 are exhibited. The system with the bearing D30 undergoes a Hopf bifurcation at a value of rotational speed between 1500 and 1550 rad/s. The eigenvalues of the open loop system for every value of Ω are shown in Fig. 3.19. The gains are considered identical for all the actuators and only the middle row of actuators is moving, therefore the configuration in Fig. 2.3(b) is used.

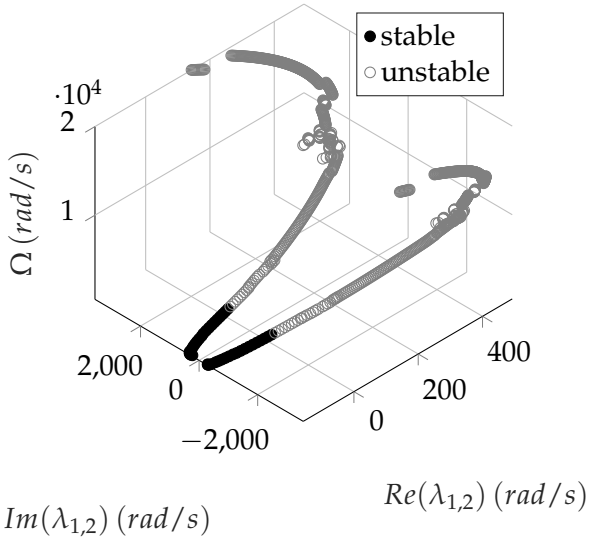

FIGURE 3.19: Eigenvalues of the open loop systems. Bearing D30

The application of a feedback control law for every Ω results in the elimination of Hopf bifurcation and the eigenvalues are placed on the negative complex half-plane, as shown in Fig. 3.20(a). The corresponding gains $\mathbf{k_i}$ are shown in Fig. 3.20(b).

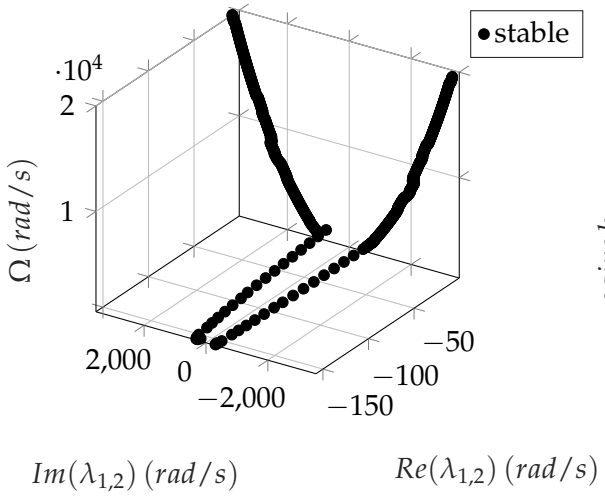

(a) Eigenvalues of the close loop systems. Bearing D30

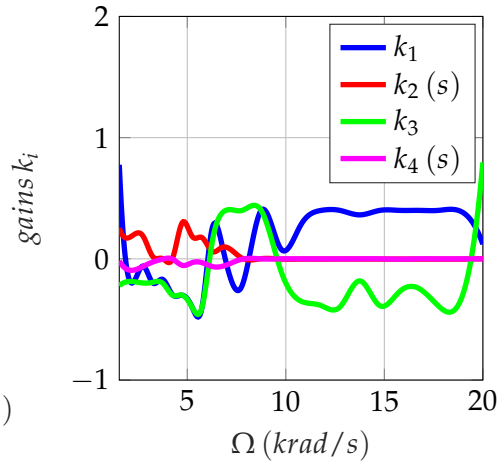

(b) gains $\mathbf{k_i}$ as a function of Ω

FIGURE 3.20: Hopf bifurcation elimination with polynomial feedback

3.3 Design Optimization for the Placement of the Equilibrium Point

In some circumstances, the placement of the equilibrium point of the rotor on a desired location is of great interest. The requirement for this can be either the avoidance of rotor-stator contact or the centralised rotor-stator configuration.

For the equilibrium point of the autonomous system to change, the actuators must be preloaded, i.e a permanent displacement of the free end of the actuators must be considered. That displacement is calculated by a design optimization procedure utilizing again the *patternsearch* function of the *Matlab Global Optimization Toolbox*. The objective function in this case is

$$min_{obj} = |x_j^* - x_{j_d}^*| + |y_j^* - y_{j_d}^*| \tag{3.19}$$

where x_j^*, y_j^* are the equilibrium displacements of the center of the disc and $x_{j_d}^*$, $y_{j_d}^*$ are the desired equilibrium displacements.

In this case, only the bearing D30 is considered. The results are identical for the bearing D100. The displacement of the actuators is symmetrical about the middle row and the actuators are numbered according to their position. The actuators on the front plane are numbered from 1 to 4 from the left to the right, on the middle plane from 5 to 8 and on the rear plane from 9 to 12 accordingly. The front plane is the third row of actuators shown in Fig. 2.4. The goal is to place the equilibrium displacements on the origin $O(0, 0)$. The necessary displacements are shown in Fig. 3.21.

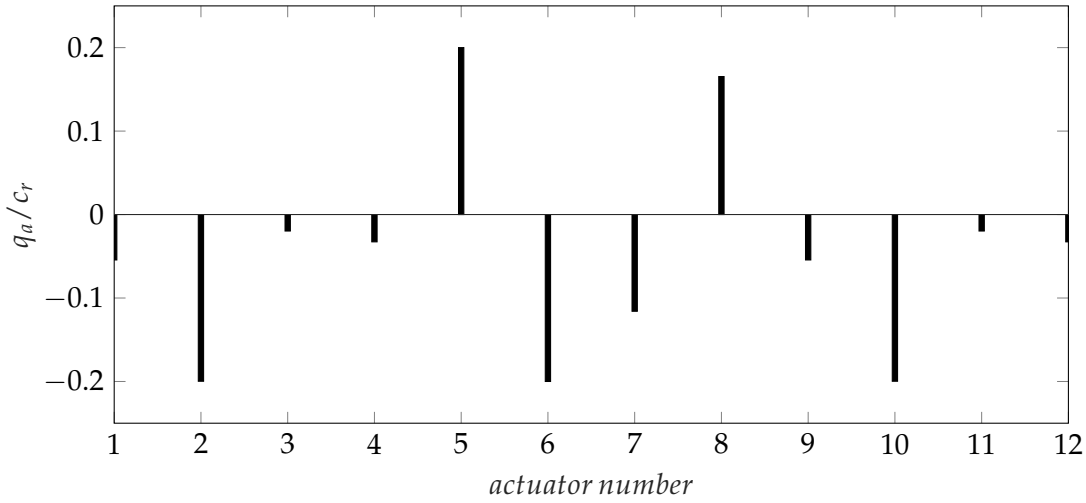

FIGURE 3.21: Displacement of the actuators in order to place the equilibrium point of the balanced system on $O(0,0)$. Bearing D30

The new equilibrium point is unstable. In order to stabilize it, a polynomial feedback law is used. The chosen setting time in this case is $t = 0.2\,s$ and the results are shown in Fig. 3.25. The orbit of the closed loop system is shown in Fig. 3.23. The shape of the foil corresponds to the equilibrium state.

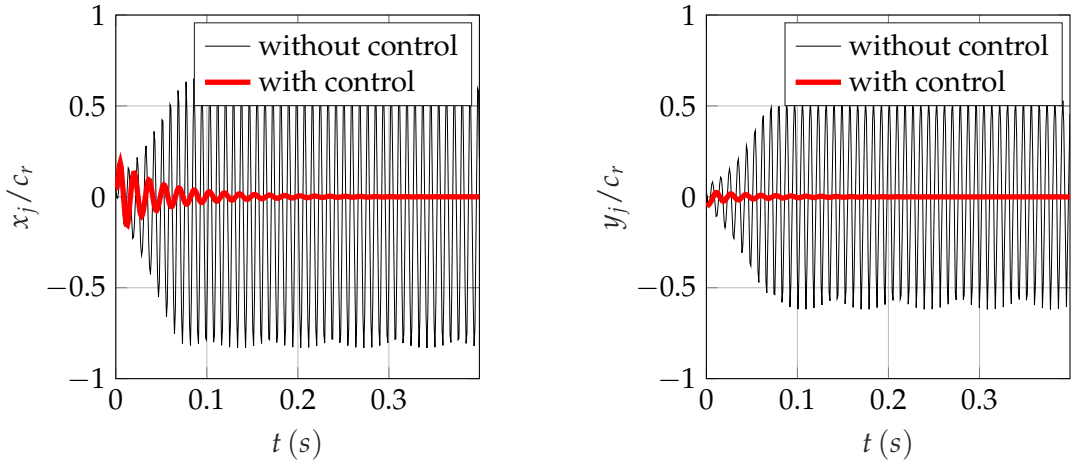

(a) x-displacement

(b) y-displacement

FIGURE 3.22: x (a) and y (b) displacement of the center of the disc of the open and close loop system at $\Omega = 1550\,rad/s$. Bearing D30. Disc mass $m_d = 0.1\,kg$. Balanced rotor

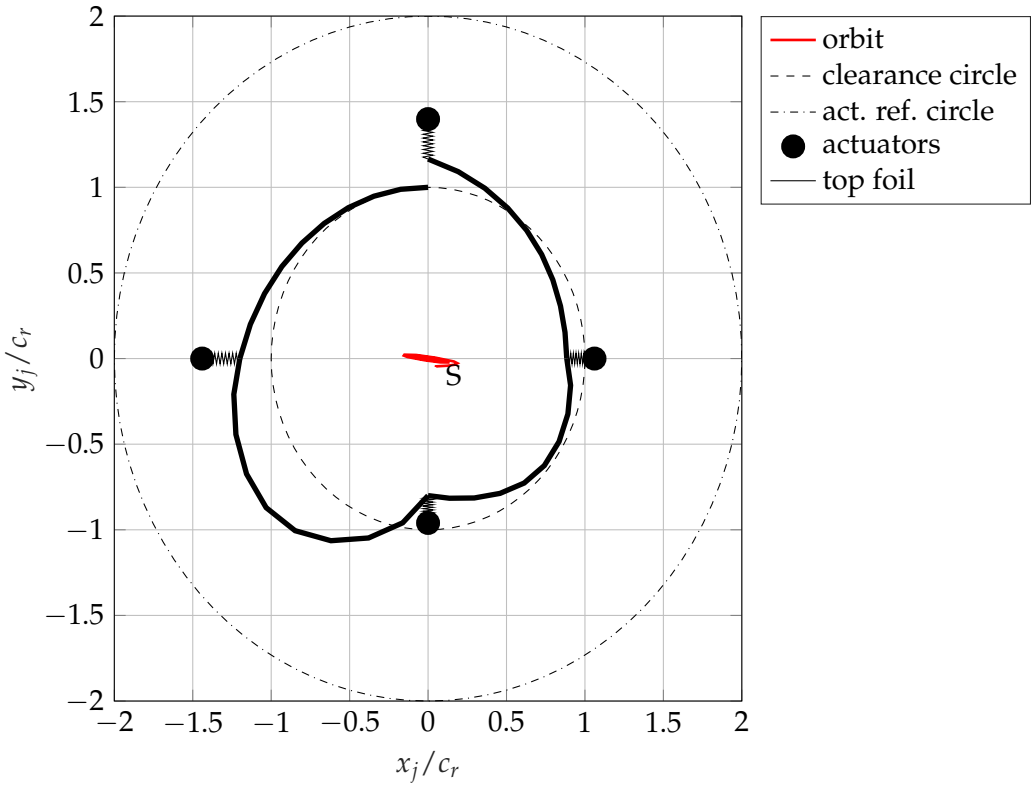

FIGURE 3.23: Orbit of the center of the disc at $\Omega = 1550 rad\,sec$. Bearing D100. Balanced rotor. The shape of the top foil corresponds to the mid plane at the equilibrium state

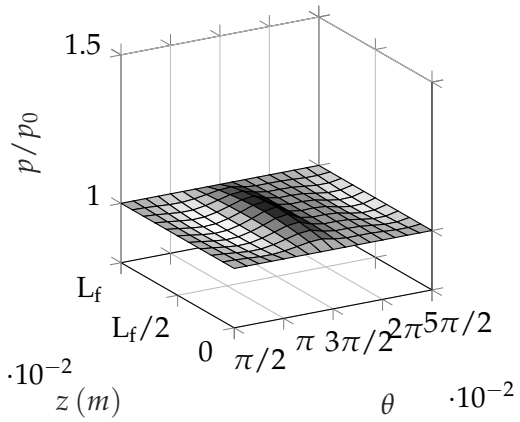

(a) pressure distribution

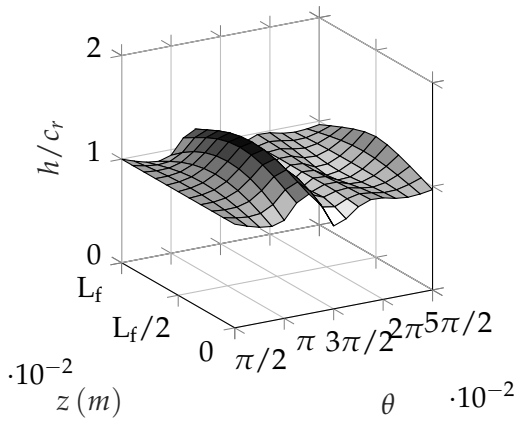

(b) film thickness

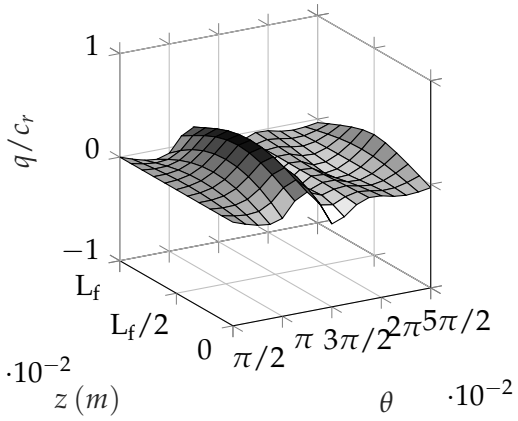

(c) foil deformation

FIGURE 3.24: Stable equilibrium pressure distribution (a), film thickness (b) and foil deformation (c) at $\Omega = 1550\,rad/s$. Bearing D30. Disc mass $m_d = 0.1\,kg$. Balanced rotor

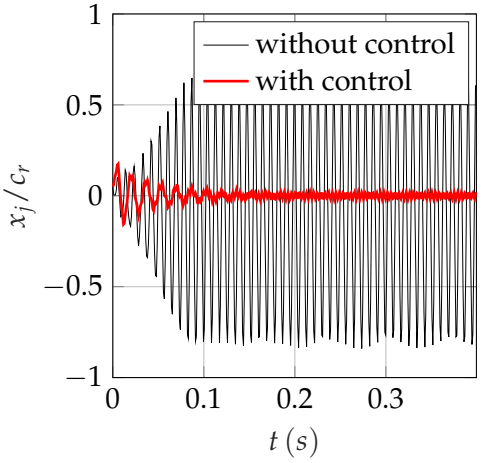

(a) x-displacement

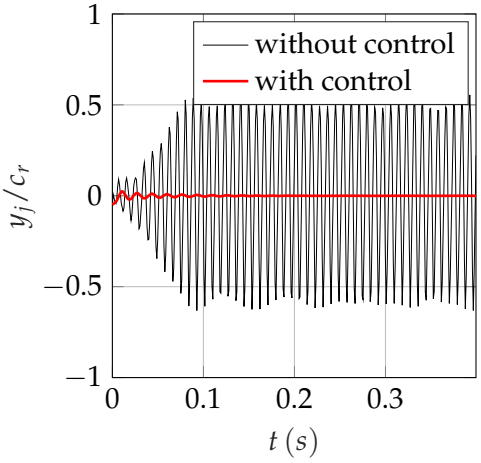

(b) y-displacement

FIGURE 3.25: x (a) and y (b) displacement of the center of the disc of the open and close loop system at $\Omega = 1550\,rad/s$. Bearing D30. Disc mass $m_d = 0.1\,kg$. Unbalance grade G2.5

Chapter 4

Conclusions and Future Work

In conclusion, it was observed that the modeling of the full dynamic system is of particular interest. The number of finite elements that can be applied in the foil structure analysis is large, but a finite element must be chosen so that the computational cost is not increased, and to focus on the accurate prediction of the radial displacements of the foil, introducing as few additional degrees of freedom (in other directions) as possible. Thin plate bending elements are ideal for this purpose. Furthermore, simple supports, e.g. actuators, have to be used if the bump foil structure is not included as it happen in conventional GFB design. Concerning the design of feedback control laws, linear polynomial feedback and classic linear control theory are found to be adequate for the stabilization of fixed points. For the elimination of Hopf Bifurcations and the stabilization of the system around fixed points, the gains must be chosen in a way that a specification, like the setting time, is satisfied. It is found that, evaluating the gains though an optimization problem is sufficient to achieve the desired response in terms of stability and time constants. In addition to this, nonlinear terms can be used in the feddback function, in order to control the amplitude and the minimal period of self-excited limit cycle motion of the balanced or the ubalanced system. This is future work to be performed.

Appendix A

Guyan Reduction

The equilibrium of a statitic problem is expressed as:

$$\mathbf{K}\boldsymbol{x} = \boldsymbol{f} \tag{A.1}$$

where $\mathbf{K}$ is the stiffness matrix, $\boldsymbol{f}$ is the force vector and $\boldsymbol{x}$ the displacement vector. By partitioning the above system of linear equations with regards to loaded-master and unloaded-slave degrees of freedom, the static equilibrium equation can be written as:

$$\begin{bmatrix} \mathbf{K}_{mm} & \mathbf{K}_{ms} \\ \mathbf{K}_{sm} & \mathbf{K}_{ss} \end{bmatrix} \begin{Bmatrix} \boldsymbol{x}_m \\ \boldsymbol{x}_s \end{Bmatrix} = \begin{Bmatrix} \boldsymbol{f}_m \\ \mathbf{0} \end{Bmatrix} \tag{A.2}$$

Solving the lower part of the above system of equations it follows:

$$\mathbf{K}_{sm}\boldsymbol{x}_m + \mathbf{K}_{ss}\boldsymbol{x}_s = 0 \tag{A.3}$$

Solving the above equation in terms of the master DOFs leads to:

$$\boldsymbol{x}_s = -\mathbf{K}_{ss}^{-1}\mathbf{K}_{sm}\boldsymbol{x}_m \tag{A.4}$$

Finally substituting to the upper partition of equation A.2 leads to the following reduced system.

$$(\mathbf{K}_{mm} - \mathbf{K}_{ms}\mathbf{K}_{ss}^{-1}\mathbf{K}_{sm})\boldsymbol{x}_m = \boldsymbol{f}_m \tag{A.5}$$

The above system of linear equations is equivalent to the original problem but expressed in terms of the master degrees of freedom. Thus, the Guyan reduction results in a reduced system by condensing away the slave degrees of freedom.

The Guyan reduction can also be expressed as a change of basis which produces a low-dimensional representation of the original space, represented by the master degrees of freedom. The linear transformation that maps the reduced space onto the full space is expressed as:

$$\begin{Bmatrix} \boldsymbol{x}_m \\ \boldsymbol{x}_s \end{Bmatrix} = \begin{bmatrix} \mathbf{I} \\ -\mathbf{K}_{ss}^{-1}\mathbf{K}_{sm} \end{bmatrix} \{\boldsymbol{x}_m\} = \{\boldsymbol{T}_G\} \{\boldsymbol{x}_m\} \tag{A.6}$$

where $\boldsymbol{T}_r$ represents the Guyan reduction transformation matrix. Thus, the reduced problem is represented as:

$$\mathbf{K}_r\boldsymbol{x}_m = \boldsymbol{f}_m \tag{A.7}$$

where $\mathbf{K}_r$ represents the reduced system of linear equations that's obtained by applying the Guyan reduction transformation on the full system, which is expressed as:

$$\mathbf{K}_r = \boldsymbol{T}_r^T \mathbf{K} \boldsymbol{T}_r \tag{A.8}$$

Appendix B

Ackermann's Theory

Suppose the open loop system

$$\begin{aligned} \dot{\mathbf{x}} &= \mathbf{A} \cdot \mathbf{x} + \mathbf{B} \cdot \mathbf{u} \\ \mathbf{y} &= \mathbf{C} \cdot \mathbf{x} \end{aligned} \tag{B.1}$$

where $\mathbf{x} \in \mathbb{R}^N$ is the state vector, $\mathbf{u} \in \mathbb{R}^M$ is the input vector and $\mathbf{y} \in \mathbb{R}^p$ is the output vector. Furthermore, $\mathbf{A} \in \mathbb{R}^{N \times N}$, $\mathbf{B} \in \mathbb{R}^{N \times M}$, $\mathbf{C} \in \mathbb{R}^{p \times N}$.

The system is controllable if the matrix

$$\mathbf{P} = \begin{bmatrix} \mathbf{B} & \mathbf{A} \cdot \mathbf{B} & ... & \mathbf{A}^{N-1} \cdot \mathbf{B} \end{bmatrix} \tag{B.2}$$

has rank N. The system is observable if the matrix

$$\mathbf{Q} \begin{bmatrix} \mathbf{C} \\ \mathbf{C} \cdot \mathbf{A} \\ ... \\ \mathbf{C} \cdot \mathbf{A}^{N-1} \end{bmatrix} \tag{B.3}$$

has rank N.

If the system is controllable, the eigenvalues of the close loop system can be placed on the desired location using the feedback control law $\mathbf{u} = -\mathbf{K} \cdot \mathbf{x}$, where the matrix $\mathbf{K}$ is calculated by the Ackermann's formula:

$$\mathbf{K} = \begin{bmatrix} 0 & 0 & ... & 1 \end{bmatrix} \cdot \mathbf{P}^{-1} \cdot g(\mathbf{A}) \tag{B.4}$$

where

$$g(s) = (s - s_1)(s - s_2)...(s - s_N) \tag{B.5}$$

is the desired characteristic polynomial and s_i are the desired eigenvalues of the close loop system.

If the system is observable, the eigenvalues of the observer can be placed in the desired location by introducing the matrix $\mathbf{L}$ as

$$\mathbf{L} = h(\mathbf{A}) \cdot \mathbf{Q}^{-1} \cdot \begin{bmatrix} 0 & 0 & ... & 1 \end{bmatrix}^T \tag{B.6}$$

where

$$h(z) = (z - z_1)(z - z_2)...(z - z_N) \tag{B.7}$$

is the desired characteristic polynomial of the observer and z_i are the desired eigenvalues of the observer.

The transformation of the system of state equations is performed by applying an eigenvalue decomposition of the matrix $\mathbf{A} = \mathbf{T_b} \cdot \mathbf{A_b} \cdot \mathbf{T_b}^{-1}$. Therefore, the transformation $\mathbf{x} = \mathbf{T_b} \cdot \mathbf{x_b}$ results in the system

$$\begin{aligned} \dot{\mathbf{x}}_\mathbf{b} &= \mathbf{A_b} \cdot \mathbf{x_b} + \mathbf{B_b} \cdot \mathbf{q_a} \\ \mathbf{y} &= \mathbf{C_b} \cdot \mathbf{x_b} \end{aligned} \tag{B.8}$$

By applying a reenlistment of the state variables, the stable and unstable subsystems are separated and can be treated independently of each other.

Bibliography

[1] Tim Leister, Christoph Baum, and Wolfgang Seemann. "On the Importance of Frictional Energy Dissipation in the Prevention of Undesirable Self-Excited Vibrations in Gas Foil Bearing Rotor Systems". In: *Technische Mechanik* 37 (June 2017), pp. 280–290. DOI: 10.24352/UB.OVGU-2017-104 (cit. on p. 1).

[2] H. Heshmat, J. A. Walowit, and O. Pinkus. "Analysis of Gas-Lubricated Foil Journal Bearings". In: *Journal of Lubrication Technology* 105.4 (Oct. 1983), pp. 647–655. ISSN: 0022-2305. DOI: 10.1115/1.3254697. eprint: https://asmedigitalcollection.asme.org/tribology/article-pdf/105/4/647/5759908/647_1.pdf. URL: https://doi.org/10.1115/1.3254697 (cit. on p. 1).

[3] Samuel Howard et al. "Gas Foil Bearing Technology Advancements for Closed Brayton Cycle Turbines". In: *AIP Conference Proceedings* 880 (Jan. 2007), pp. 668–680. DOI: 10.1063/1.2437506 (cit. on p. 1).

[4] Samuel A. Howard. "Rotordynamics and Design Methods of an Oil-Free Turbocharger©". In: *Tribology Transactions* 42.1 (1999), pp. 174–179. DOI: 10.1080/10402009908982205. eprint: https://doi.org/10.1080/10402009908982205. URL: https://doi.org/10.1080/10402009908982205 (cit. on p. 1).

[5] C. Dellacorte, A. R. Zaldana, and K. C. Radil. "A Systems Approach to the Solid Lubrication of Foil Air Bearings for Oil-Free Turbomachinery". In: *Journal of Tribology* 126.1 (2004), pp. 200–207 (cit. on p. 1).

[6] W. A. Gross. "Paper 9: Gas Bearings: Journal and Thrust". In: *Proceedings of the Institution of Mechanical Engineers, Conference Proceedings* 182.1 (1967), pp. 116–150. DOI: 10.1243/PIME_CONF_1967_182_012_02. eprint: https://doi.org/10.1243/PIME_CONF_1967_182_012_02. URL: https://doi.org/10.1243/PIME_CONF_1967_182_012_02 (cit. on p. 1).

[7] C. A. Heshmat and H. Heshmat. "An Analysis of Gas-Lubricated, Multileaf Foil Journal Bearings With Backing Springs". In: *Journal of Tribology* 117.3 (July 1995), pp. 437–443. ISSN: 0742-4787. DOI: 10.1115/1.2831272. eprint: https://asmedigitalcollection.asme.org/tribology/article-pdf/117/3/437/5938258/437_1.pdf. URL: https://doi.org/10.1115/1.2831272 (cit. on p. 2).

[8] M.J. Braun et al. "Two-dimensional dynamic simulation of a continuous foil bearing". In: *Tribology International* 29.1 (1996), pp. 61–68. ISSN: 0301-679X. DOI: https://doi.org/10.1016/0301-679X(95)00035-3. URL: https://www.sciencedirect.com/science/article/pii/0301679X95000353 (cit. on p. 2).

[9] H. Heshmat, W. Shapiro, and S. Gray. "Development of Foil Journal Bearings for High Load Capacity and High Speed Whirl Stability". In: *Journal of Lubrication Technology* 104.2 (Apr. 1982), pp. 149–156. ISSN: 0022-2305. DOI: 10.1115/1.3253173. eprint: https://asmedigitalcollection.asme.org/tribology/article-pdf/104/2/149/5690138/149_1.pdf. URL: https://doi.org/10.1115/1.3253173 (cit. on p. 2).

[10] H. Chen et al. “Application of foil bearings to helium turbocompressor”. In: (Jan. 2001) (cit. on p. 2).

[11] Krzysztof Nalepa, Paweł Pietkiewicz, and Żywica Grzegorz. “Development of the foil bearing technology”. In: *Technical Sciences* No. 12 (Nov. 2009), pp. 229–240. DOI: 10.2478/v10022-009-0019-2 (cit. on pp. 2, 3).

[12] Christopher Dellacorte and John Carter Wood. “High Temperature Solid Lubricant Materials for Heavy Duty and Advanced Heat Engines”. In: 1994 (cit. on p. 2).

[13] A. B. Palazzolo et al. “Test and Theory for Piezoelectric Actuator-Active Vibration Control of Rotating Machinery”. In: *Journal of Vibration and Acoustics* 113.2 (Apr. 1991), pp. 167–175. ISSN: 1048-9002. DOI: 10.1115/1.2930165. eprint: https://asmedigitalcollection.asme.org/vibrationacoustics/article-pdf/113/2/167/5716477/167_1.pdf. URL: https://doi.org/10.1115/1.2930165 (cit. on p. 3).

[14] Stuart Bennett. “Nicholas Minorsky and the automatic steering of ships”. In: *IEEE Control Systems Magazine* 4 (1984), pp. 10–15 (cit. on p. 4).

[15] Theodore Psonis, Pantelis Nikolakopoulos, and Epaminondas Mitronikas. “Design of a PID Controller for a Linearized Magnetic Bearing”. In: *International Journal of Rotating Machinery* 2015 (Oct. 2015), pp. 1–12. DOI: 10.1155/2015/656749 (cit. on p. 4).

[16] John Y Hung, Nathaniel G Albritton, and Fan Xia. “Nonlinear control of a magnetic bearing system”. In: *Mechatronics* 13.6 (2003), pp. 621–637. ISSN: 0957-4158. DOI: https://doi.org/10.1016/S0957-4158(02)00034-X. URL: https://www.sciencedirect.com/science/article/pii/S095741580200034X (cit. on p. 4).

[17] Jisu Park and Kyuho Sim. “A Feasibility Study of Controllable Gas Foil Bearings With Piezoelectric Materials Via Rotordynamic Model Predictions”. In: *Journal of Engineering for Gas Turbines and Power* 141 (Sept. 2018). DOI: 10.1115/1.4041384 (cit. on p. 5).

[18] Leonid Savin, Denis Shutin, and A Kuzavka. “Actuators of active tribotechnical systems of the rotor-bearing type”. In: *IOP Conference Series: Materials Science and Engineering* 233 (Aug. 2017), p. 012043. DOI: 10.1088/1757-899X/233/1/012043 (cit. on p. 5).

[19] Sebastian von Osmanski and Ilmar F. Santos. “Gas foil bearings with radial injection: Multi-domain stability analysis and unbalance response”. In: *Journal of Sound and Vibration* 508 (2021), p. 116177. ISSN: 0022-460X. DOI: https://doi.org/10.1016/j.jsv.2021.116177. URL: https://www.sciencedirect.com/science/article/pii/S0022460X21002492 (cit. on p. 6).

[20] Sebastian von Osmanski and Ilmar F. Santos. “Gas foil bearings with radial injection: Multi-domain stability analysis and unbalance response”. In: *Journal of Sound and Vibration* 508 (2021), p. 116177. ISSN: 0022-460X. DOI: https://doi.org/10.1016/j.jsv.2021.116177. URL: https://www.sciencedirect.com/science/article/pii/S0022460X21002492 (cit. on p. 6).

[21] Su-Huan Chen and HH Pan. “Guyan reduction”. In: *Communications in applied numerical methods* 4.4 (1988), pp. 549–556 (cit. on pp. 6, 9).

[22] O. S. Reynolds. *Hydrodynamic Lubrication*. Springer-Verlag, 2006 (cit. on p. 6).

[23] "Elastic Thin Shell". In: *The Finite Element Method*. John Wiley & Sons, Ltd, 2018. Chap. 11, pp. 255–272. ISBN: 9781119107323. DOI: https://doi.org/10.1002/9781119107323.ch11. eprint: https://onlinelibrary.wiley.com/doi/pdf/10.1002/9781119107323.ch11. URL: https://onlinelibrary.wiley.com/doi/abs/10.1002/9781119107323.ch11 (cit. on p. 9).

[24] "Elastic Thin Plate". In: *The Finite Element Method*. John Wiley & Sons, Ltd, 2018. Chap. 10, pp. 223–253. ISBN: 9781119107323. DOI: https://doi.org/10.1002/9781119107323.ch10. eprint: https://onlinelibrary.wiley.com/doi/pdf/10.1002/9781119107323.ch10. URL: https://onlinelibrary.wiley.com/doi/abs/10.1002/9781119107323.ch10 (cit. on p. 9).

[25] Christoph Baum et al. "A computationally efficient nonlinear foil air bearing model for fully coupled, transient rotor dynamic investigations". In: *Tribology International* 153 (2021), p. 106434. ISSN: 0301-679X. DOI: https://doi.org/10.1016/j.triboint.2020.106434. URL: https://www.sciencedirect.com/science/article/pii/S0301679X20302711 (cit. on pp. 9, 14, 15).

[26] Jozef Hanc, Edwin Taylor, and Slavomir Tuleja. "Deriving Lagrange's equations using elementary calculus". In: *American Journal of Physics - AMER J PHYS* 72 (Apr. 2004), pp. 510–513. DOI: 10.1119/1.1603270 (cit. on p. 9).

[27] *MATLAB Optimization Toolbox*. The MathWorks, Natick, MA, USA. <The year of your version, you can find it out using ver> (cit. on p. 9).

[28] Otto T. Bruhns. "Plates and Shells". In: *Advanced Mechanics of Solids*. Berlin, Heidelberg: Springer Berlin Heidelberg, 2003, pp. 131–148. ISBN: 978-3-662-05271-6. DOI: 10.1007/978-3-662-05271-6_8. URL: https://doi.org/10.1007/978-3-662-05271-6_8 (cit. on p. 9).

[29] Philip E. Gustafson and Brian A. Hagler. "Gaussian quadrature rules and numerical examples for strong extensions of mass distribution functions". In: *Journal of Computational and Applied Mathematics* 105.1 (1999), pp. 317–326. ISSN: 0377-0427. DOI: https://doi.org/10.1016/S0377-0427(99)00023-0. URL: https://www.sciencedirect.com/science/article/pii/S0377042799000230 (cit. on p. 9).

[30] Sanjit Mohanty and Rajani Ballav Dash. "A quadrature rule of Lobatto-Gaussian for numerical integration of analytic functions". In: *Numerical Algebra, Control & Optimization* (Jan. 2021). DOI: 10.3934/naco.2021031 (cit. on p. 12).

[31] George Ellis. "Introduction to Observers in Control Systems". In: Dec. 2012, pp. 185–212. ISBN: 9780123859204. DOI: 10.1016/B978-0-12-385920-4.00010-2 (cit. on p. 29).

[32] Peiyu and Guanrongchen. "HOPF BIFURCATION CONTROL USING NONLINEAR FEEDBACK WITH POLYNOMIAL FUNCTIONS". In: *International Journal of Bifurcation and Chaos* 14 (Nov. 2011). DOI: 10.1142/S0218127404010291 (cit. on pp. 29, 37, 38).

[33] *The Hopf Bifurcation and Its Applications*. 1976 (cit. on pp. 29, 37).

[34] Chutiphon Pukdeboon. "A Review of Fundamentals of Lyapunov Theory". In: *J Appl Sci* 10 (Jan. 2011) (cit. on p. 29).

[35] K. Nordstrom and H. Norlander. "On the multi input pole placement control problem". In: *Proceedings of the 36th IEEE Conference on Decision and Control*. Vol. 5. 1997, 4288–4293 vol.5. DOI: 10.1109/CDC.1997.649511 (cit. on p. 31).